LMECA2660 - Project
Simulating 2D flow around an oscillating obstacle

DEGROOFF Vincent – NOMA : 09341800

Friday, 6 may 2022

1 Problem statement

In this project, we are asked to solve the Navier-Stokes equations for incompressible flows in 2 dimensions, passed a rectangular obstacle. The geometry of the problem is described with more details in figure 1.
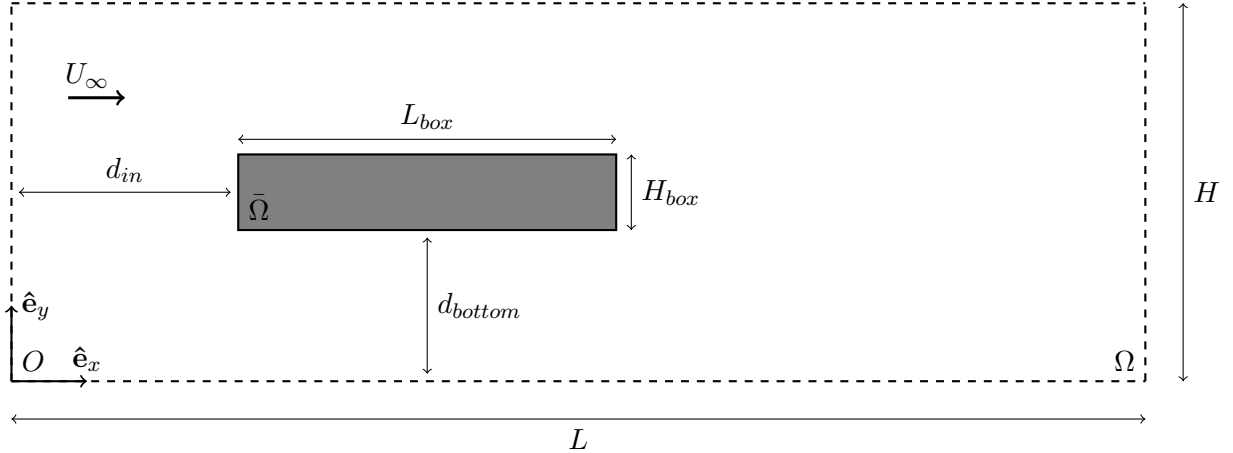

Figure 1. Description of the case studied. (Image courtesy of Pierre Balty)

In the rest of this document, we will only work with dimensionless variables. Hence, it might be useful to precise the choice of nondimensionalization. Dimensionless quantities are noted here with an asterisk superscript, the position vector is $\mathbf{x} = (x, y)$ and the velocity vector is $\mathbf{v} = (u, v)$.

$$\mathbf{x}^* = \frac{\mathbf{x}}{H_{box}} \qquad \mathbf{v}^* = \frac{\mathbf{v}}{U_\infty} \qquad t^* = \frac{tU_\infty}{H_{box}} \qquad p^* = \frac{p - p_{ref}}{\rho U_\infty^2} \qquad T^* = \frac{T - T_{ref}}{\Delta T} \tag{1}$$

We can also define dimensionless numbers, using physical properties of the fluid: its kinematic viscosity ν, its thermal diffusivity α, its heat capacity c_p, its density ρ_0, and its the volumetric thermal expansion coefficient $\beta = \frac{1}{\rho_0} \left(\frac{\partial \rho}{\partial T} \right)_p$.

$$Re = \frac{U_\infty H_{box}}{\nu} \qquad Pr = \frac{\nu}{\alpha} \qquad Gr = \frac{\beta \Delta T g H_{box}^3}{\nu^2} \qquad Ec = \frac{U_\infty}{c_p \Delta T} \tag{2}$$

where g is the gravitational acceleration.

We can now state the Navier-Stokes equations in dimensionless form, using the Boussinesq approximation, for a domain Ω moving uniformly at velocity $\mathbf{v}_{mesh}$. **From this point in the document, we will drop this asterisk for the sake of readability**.

$$\frac{\partial u}{\partial x} + \frac{\partial v}{\partial y} = 0 \qquad \text{Mass cons.} \qquad (3)$$

$$\frac{\partial u}{\partial t} + \bar{u}\frac{\partial u}{\partial x} + \bar{v}\frac{\partial u}{\partial y} = -\frac{\partial p}{\partial x} + \frac{1}{Re}\left(\frac{\partial^2 u}{\partial x^2} + \frac{\partial^2 u}{\partial y^2}\right) \qquad \text{Momentum in } \hat{\mathbf{e}}_x \qquad (4)$$

$$\frac{\partial v}{\partial t} + \bar{u}\frac{\partial v}{\partial x} + \bar{v}\frac{\partial v}{\partial y} = -\frac{\partial p}{\partial y} + \frac{1}{Re}\left(\frac{\partial^2 v}{\partial x^2} + \frac{\partial^2 v}{\partial y^2}\right) + \frac{Gr}{Re^2}T \qquad \text{Momentum in } \hat{\mathbf{e}}_y \qquad (5)$$

$$\frac{\partial T}{\partial t} + \bar{u}\frac{\partial T}{\partial x} + \bar{v}\frac{\partial T}{\partial y} = \frac{1}{Re\,Pr}\left(\frac{\partial^2 T}{\partial x^2} + \frac{\partial^2 T}{\partial y^2}\right) + \frac{Ec}{Re}\phi \qquad \text{Energy cons.} \qquad (6)$$

Where $\bar{u} = u - u_{mesh}$, $\bar{v} = v - v_{mesh}$ and the viscous dissipation ϕ is defined as follows:

$$\phi = 2\mu\,\mathbf{d} : \mathbf{d} = 2\left[\left(\frac{\partial u}{\partial x}\right)^2 + \left(\frac{\partial v}{\partial y}\right)^2\right] + \left(\frac{\partial u}{\partial y} + \frac{\partial v}{\partial x}\right)^2 \qquad \text{with} \qquad \mathbf{d} = \frac{1}{2}\left[(\nabla u) + (\nabla u)^T\right] \qquad (7)$$

2   Obstacle oscillation model

The rectangular obstacle stays at its initial position in the x direction until a time t_0, where it starts oscillating horizontally. The same happens in the y direction, where the threshold time $= \tilde{t}_0$.

The dimensionless position of the obstacle is then given by:

$$\begin{aligned}
x_{mesh}(t) - x_{mesh}(t_0) &= \kappa\left[1 - \cos\left(2\pi S_t(t - t_0)\right)\right] & t_0 \leq t \\
y_{mesh}(t) - y_{mesh}(\tilde{t}_0) &= \tilde{\kappa}\left[1 - \cos\left(2\pi \tilde{S}_t(t - \tilde{t}_0)\right)\right] & \tilde{t}_0 \leq t
\end{aligned} \qquad (8)$$

However, in our model, we need to impose the velocity as boundary condition:

$$\begin{aligned}
u_{mesh}(t) &= \kappa(2\pi S_t)\sin\left(2\pi S_t(t - t_0)\right) = \alpha\sin\left(2\pi S_t(t - t_0)\right) & t_0 \leq t \\
v_{mesh}(t) &= \tilde{\kappa}(2\pi \tilde{S}_t)\sin\left(2\pi \tilde{S}_t(t - \tilde{t}_0)\right) = \tilde{\alpha}\sin\left(2\pi \tilde{S}_t(t - \tilde{t}_0)\right) & \tilde{t}_0 \leq t
\end{aligned} \qquad (9)$$

Since the displacement in $\hat{\mathbf{e}}_y$ is typically used to produce a perturbation, it stops after one period. The numerical values chosen for the Strouhal number S_t and the velocity amplitude α are

$$S_t = \frac{1}{3} \qquad \tilde{S}_t = S_t \qquad \alpha = \frac{1}{2} \qquad \tilde{\alpha} = \frac{\alpha}{10} \qquad (10)$$

3   Boundary conditions

(1) The inflow velocity has an horizontal component, with a uniform profile, and no vertical component. (2) The lateral boundaries will be considered as inviscid, with a no-through flow condition and zero vorticity, except stated otherwise. (3) No-through flow and no-slip conditions are enforced at the obstacle boundaries. (4) At the outflow, we try to mimic a transparent boundary condition, by advecting the fields u, ω and T at a velocity $u_c = 1 - u_{mesh}$. (5) Except at the outflow,

the boundary conditions for temperature will be either adiabatic or Dirichlet. To be more precise, a summary of these boundary conditions is presented in table 1.

Location	First condition	Second condition	Temperature condition
Inflow	$u = 1$	$v = 0$	$\frac{\partial T}{\partial x} = 0$
Lateral walls	$u = 1$ (or $u = 0$)	$v = 0$	$\frac{\partial T}{\partial y} = 0$ or $T = T_{wall}$
Obstacle wall	$u = 0$	$v = 0$	$\frac{\partial T}{\partial n} = 0$ or $T = T_{wall}$
Outflow	$\frac{\partial u}{\partial t} + u_c \frac{\partial u}{\partial x} = 0$	$\frac{\partial \omega}{\partial t} + u_c \frac{\partial \omega}{\partial x} = 0$	$\frac{\partial T}{\partial t} + u_c \frac{\partial T}{\partial x} = 0$

Table 1. Boundary conditions of the dimensionless fields.

4 Numerical solver

The Navier-stokes equations shown in (3)-(6) are integrated in time using a two-step projection scheme that ensures a divergence-free velocity field **v**. As often with finite difference method for Navier-Stokes equations, the fields u, v, p, ω and T are discretized using a staggered MAC mesh which is represented in figure 2. In this project, we use a uniform grid with $\Delta x = \Delta y = h$, but a non-uniform grid with stretching would be more adapted. It would allow us to have a finer grid near the walls and a coarser mesh where the flow is irrotational.

When a boundary condition must be applied at some position **x** where a field is not defined, we define *ghost points* outside the domain in order to facilitate the update of the values of u, v and T inside the domain. The value of these ghost points is a linear combination of values further inside the domain, whose weights are found with Taylor series.
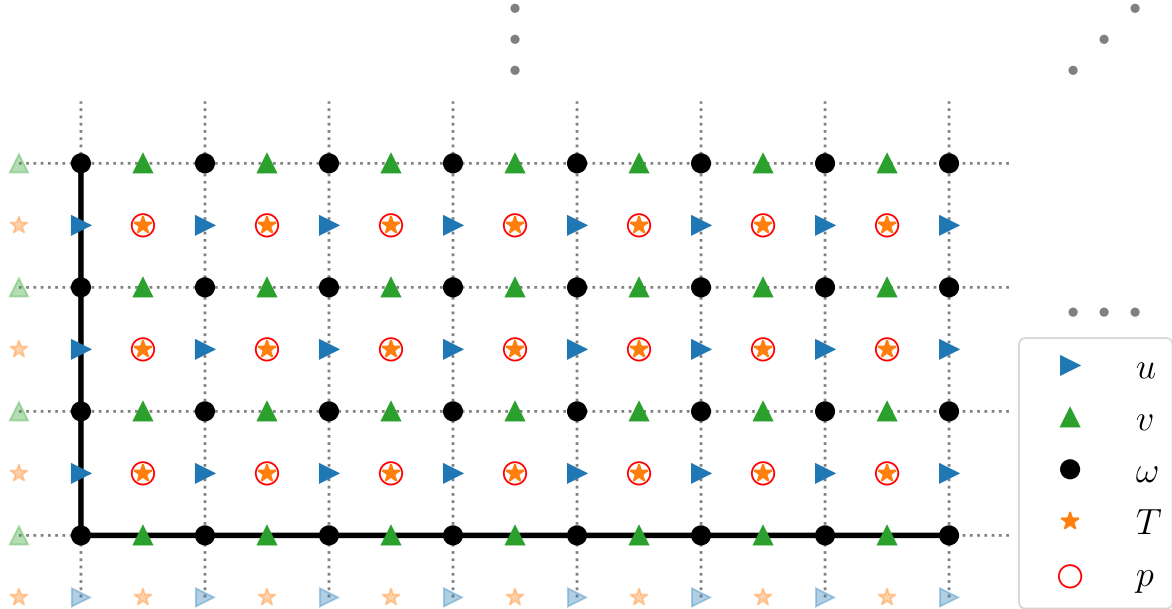

Figure 2. Staggered MAC mesh near a rectangular corner of the domain Ω. Ghost points are more transparent than regular points.

3

Concerning the time integration, the convective term is integrated using the explicit and second order Adams-Bashforth scheme (explicit Euler scheme for the first time step), while the diffusive term is handled using the explicit and first order Euler scheme. The solver proposed can also handle the diffusive term for $\mathbf{v}$ with a Crank-Nicolson scheme. This is done with an ADI method in order to only solve tri-diagonal systems. However, this implicit method was not implemented for the temperature field, and is not assured to be second order at the boundaries.

First, we compute the convective terms $\mathbf{H} = (H_x, H_y)$ that discretize $(\boldsymbol{\nabla}\mathbf{v}) \cdot (\mathbf{v} - \mathbf{v}_{mesh})$, and H_T discretizing $(\boldsymbol{\nabla}T) \cdot (\mathbf{v} - \mathbf{v}_{mesh})$. Second, we perform a predictor step to obtain an intermediate field denoted $\mathbf{v}^*$. Third, we solve the Poisson equation for Φ, using the PETSc library [1]. Finally, we obtain the next iterates once the corrector step is completed. This procedure is detailed in equations (11) - (15).

$$\frac{\mathbf{v}^* - \mathbf{v}^n}{\Delta t} = \frac{-1}{2}\left(3\,\mathbf{H}^n - \mathbf{H}^{n-1}\right) - \boldsymbol{\nabla}p^n + \frac{1}{Re}\nabla^2\mathbf{v}^n - \frac{Gr}{Re^2}\frac{\mathbf{g}}{\|\mathbf{g}\|}T^n \tag{11}$$

$$\nabla^2\Phi = \frac{1}{\Delta t}\,\nabla \cdot \mathbf{v}^* \tag{12}$$

$$\frac{\mathbf{v}^{n+1} - \mathbf{v}^*}{\Delta t} = -\boldsymbol{\nabla}\Phi \tag{13}$$

$$p^{n+1} = p^n + \Phi \tag{14}$$

$$T^{n+1} = \frac{-1}{2}\left(3\,H_T^n - H_T^{n-1}\right) + \frac{1}{Re\,Pr}\nabla^2 T^n + \frac{Ec}{Re}\phi^n \tag{15}$$

The convection contribution can be computed using either the advective form or the divergence form, respectively

$$\mathbf{H} = (\boldsymbol{\nabla}\mathbf{v}) \cdot (\mathbf{v} - \mathbf{v}_{mesh}) \qquad \text{or} \qquad \mathbf{H} = \boldsymbol{\nabla} \cdot \left(\mathbf{v}\left(\mathbf{v} - \mathbf{v}_{mesh}\right)\right) \tag{16}$$

It was chosen to take the average of both forms, for $\mathbf{H}$ and for H_T.

To ensure the stability of the scheme, the *Fourier number* and the *Courant-Friedrichs-Lewy number* were respectively set to [1]

$$r = \frac{\Delta t}{Re\,h^2} = 0.2 \qquad\qquad CFL = \frac{(|u| + |v|)\Delta t}{h} = 0.7 \tag{17}$$

where the velocity $(|u| + |v|)$ was estimated to 4. As an option, the program can use an adaptive time step Δt based on the maximum value of the velocity $|u| + |v|$ computed at the previous step.

5   Simulations without temperature coupling

Different cases will be considered:

1. The obstacle stays at rest. The flow is steady, but unstable.
2. The obstacle oscillates vertically during one period, starting at $\tilde{t}_0 = 0$, to break the symmetry and obtain an unsteady flow.

---

[1]Recall that the variables t, h, u and v are dimensionless, so that r and CFL are also.

3. The obstacle oscillates horizontally, starting at $t_0 = 0$.
4. The obstacle oscillates horizontally, starting at $t_0 = 0$. But we also add a vertical perturbation of one period, starting at $\tilde{t}_0 = 0$ to initiate an asymmetrical vortex shedding.

Based on the simulation of each of these cases, some analysis and visualizations will be provided: the vorticity field ω, the streamfunction ψ with its associated streamlines, the drag coefficient C_d, the lift coefficient C_l and the evolution of the mesh Reynolds number indicating the quality of the simulation.

With the expression of the vorticity in 2D

$$\omega = \nabla \times \mathbf{v} = \frac{\partial v}{\partial x} - \frac{\partial u}{\partial y} \tag{18}$$

we can easily compute ω on the staggered grid as shown previously in figure 2, using centered finite differences.

The streamfunction is defined by

$$u = \frac{\partial \psi}{\partial y} \qquad v = -\frac{\partial \psi}{\partial x} \tag{19}$$

The value $\psi(x, y)$ can therefore be computed over the whole domain Ω by integrating the differential form $d\psi = u \, dy - v \, dx = \mathbf{v} \cdot \hat{\mathbf{n}} \, ds$ along some path Γ from the reference point $(0, 0)$ to (x, y). We should note that the result is path-independent since the flow is divergence-free. In fact, if one choses another path Γ' from $(0, 0)$ to (x, y), we can obtain a closed curve C by concatenating both curves:

$$\int_{\Gamma} \mathbf{v} \cdot \hat{\mathbf{n}} \, ds + \int_{-\Gamma'} \mathbf{v} \cdot \hat{\mathbf{n}} \, ds = \oint_C \mathbf{v} \cdot \hat{\mathbf{n}} \, ds = \iint_S \nabla \cdot \mathbf{v} \, da = 0 \tag{20}$$

The drag force D and the lift force L can be computed by integrating the stress tensor $\boldsymbol{\sigma}$ on the boundary $\partial\bar{\Omega}$ of the rectangular body $\bar{\Omega}$. With dimensional variables, we have

$$\mathbf{F} = D \, \hat{\mathbf{e}}_x + L \, \hat{\mathbf{e}}_y = \int_{\partial\bar{\Omega}} \mathbf{n} \cdot \boldsymbol{\sigma} = \int_{\partial\bar{\Omega}} \mathbf{n} \cdot (-p\boldsymbol{\delta} + 2\mu\mathbf{d}) \tag{21}$$

After some simplifications, and a nondimensionalization, we obtain

$$C_d = \frac{D}{\frac{1}{2}\rho U_\infty^2} = \int_{y^-}^{y^+} \left[p(x^-, y) - p(x^+, y) \right] dy + \frac{1}{Re} \int_{x^-}^{x^+} \left[\left.\frac{\partial u}{\partial y}\right|_{(x,y^+)} - \left.\frac{\partial u}{\partial y}\right|_{(x,y^-)} \right] dx \tag{22}$$

$$C_l = \frac{L}{\frac{1}{2}\rho U_\infty^2} = \int_{x^-}^{x^+} \left[p(x, y^-) - p(x, y^+) \right] dx + \frac{1}{Re} \int_{y^-}^{y^+} \left[\left.\frac{\partial v}{\partial x}\right|_{(x^+,y)} - \left.\frac{\partial v}{\partial x}\right|_{(x^-,y)} \right] dy \tag{23}$$

where x^- and x^+ respectively refer to the x value on the left and right sides of the rectangle, and y^- and y^+ respectively refer to the y value underneath and above the rectangle.

Finally, two mesh Reynolds numbers can be computed:

$$Re_h = (|u| + |v|) \, h \, Re \qquad\qquad \text{based on the velocity of the flow} \tag{24}$$
$$Re_\omega = |\omega| \, h^2 \, Re \qquad\qquad \text{based on the vorticity of the flow} \tag{25}$$

Here, we are only interested about their maximum value over the domain Ω at each time step.

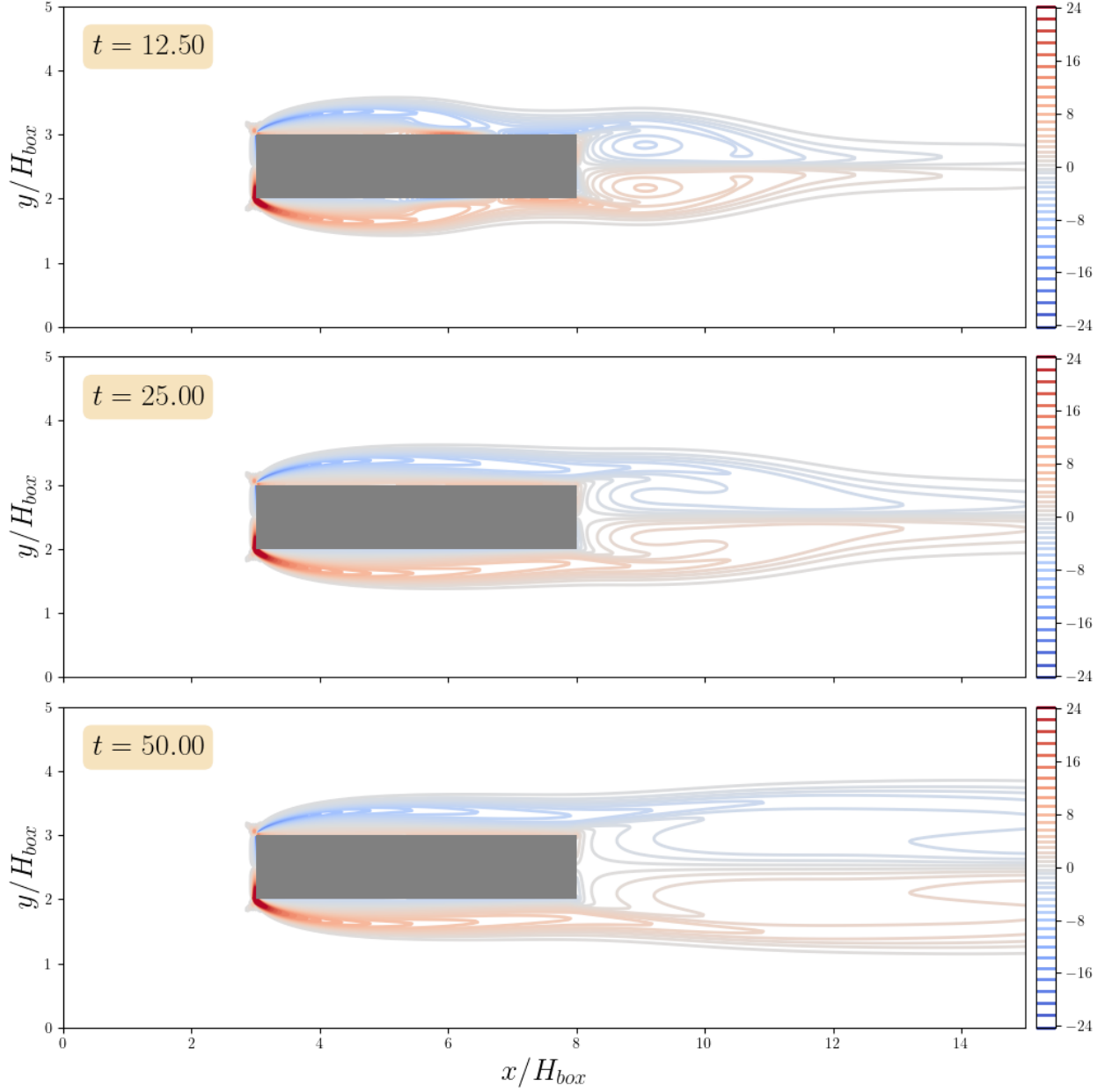## 5.1   Case 1: obstacle at rest with symmetrical flow

Figure 3. Level sets of the vorticity $\omega^* = \frac{\omega H_{box}}{U_\infty}$ in *case 1* at different dimensionless times t. These levels sets are slightly more concentrated around zero for a better visualization.

A few remarks:

- The vorticity is the highest around the left corners of the obstacle, near the inflow.
- There are two kind of recirculation regions: the first kind above and below the rectangle, and the second kind behind.
- The flow rotates clockwise ($\omega < 0$) in the boundary layer located above the obstacle, except very near the wall ($\omega > 0$), and reciprocally below the obstacle.
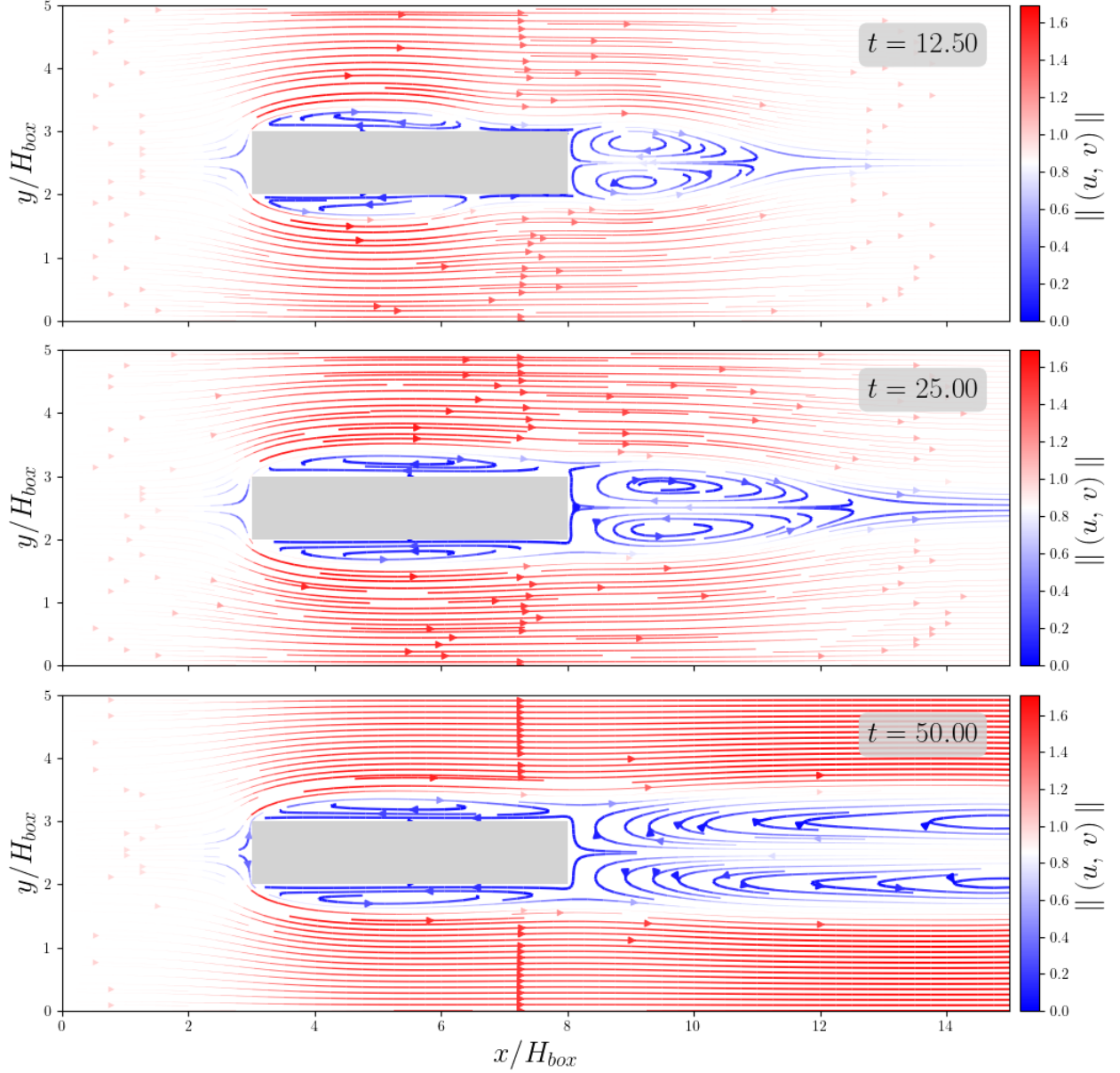
Figure 4. Snapshot of the streamlines of *case 1*. The color is proportional to the norm of the dimensionless velocity. The width of the lines is proportional to $|1 - \|\mathbf{v}\||$ in order to highlight the regions where $\mathbf{v}$ is very different than the mean-flow.

As show in figure 4, the recirculation region grows with time. The stagnation point moves from $x - x_{wall} \approx 3$ at $t = 12.5$ to $x - x_{wall} \approx 4.5$ at $t = 25.$. The flow recirculation even becomes too large for the computational domain since the stagnation point grows beyond $x = 15$ at $t \approx 40$.

The mesh Reynolds numbers are represented in figure 5. Their value quickly decrease before stabilizing around 25. This is probably due to the fact that the flow is initially nonphysical with discontinuities of u near the walls that degrade the quality of the numerical simulation.

In figure 6, the lift is zero (or almost due to numerical rounding errors) since the flow is symmetrical. On the other hand, the drag coefficient is non-zero, and $C_d \approx 1.5$ before the stagnation point leaves the domain.
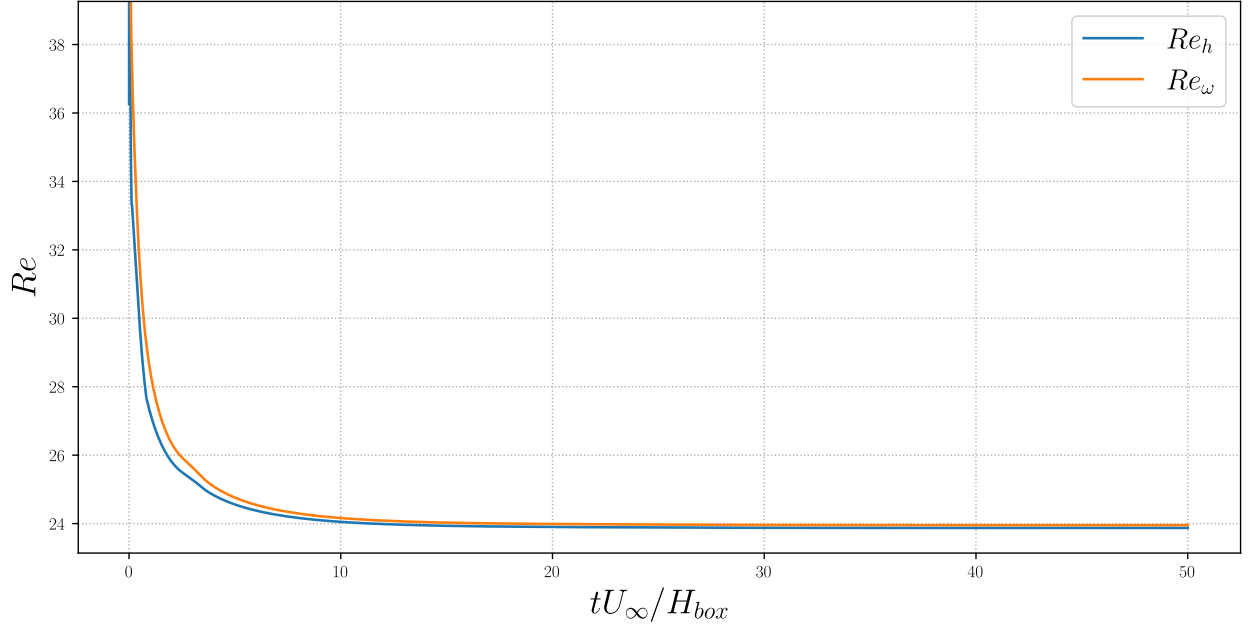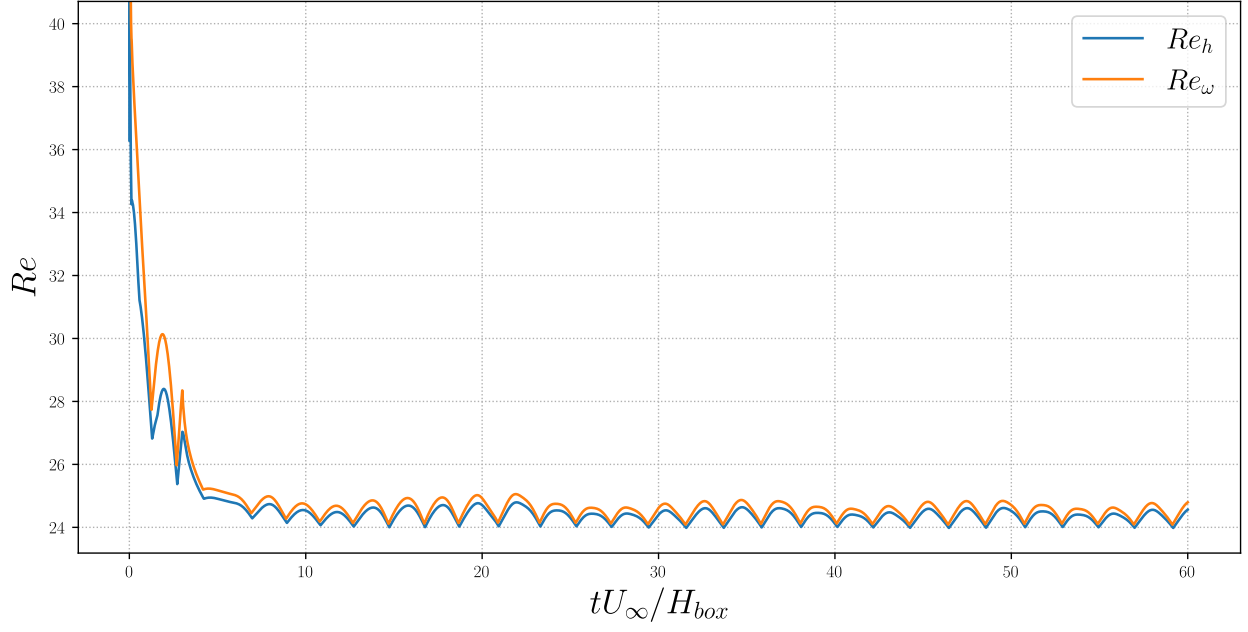
**Figure 5.** Mesh Reynolds numbers evolution for *case 1*.
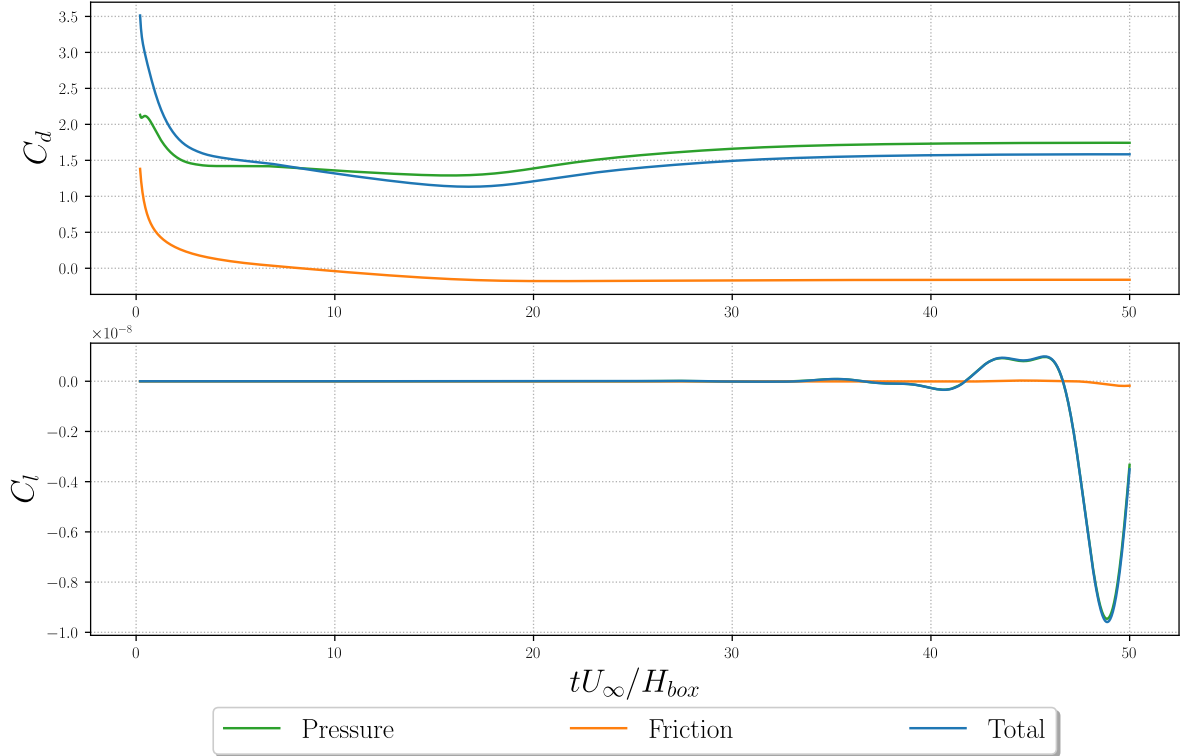
Figure 6. Aerodynamic coefficients evolution for *case 1*.

## 5.2   Case 2: obstacle at rest with unsymmetrical flow
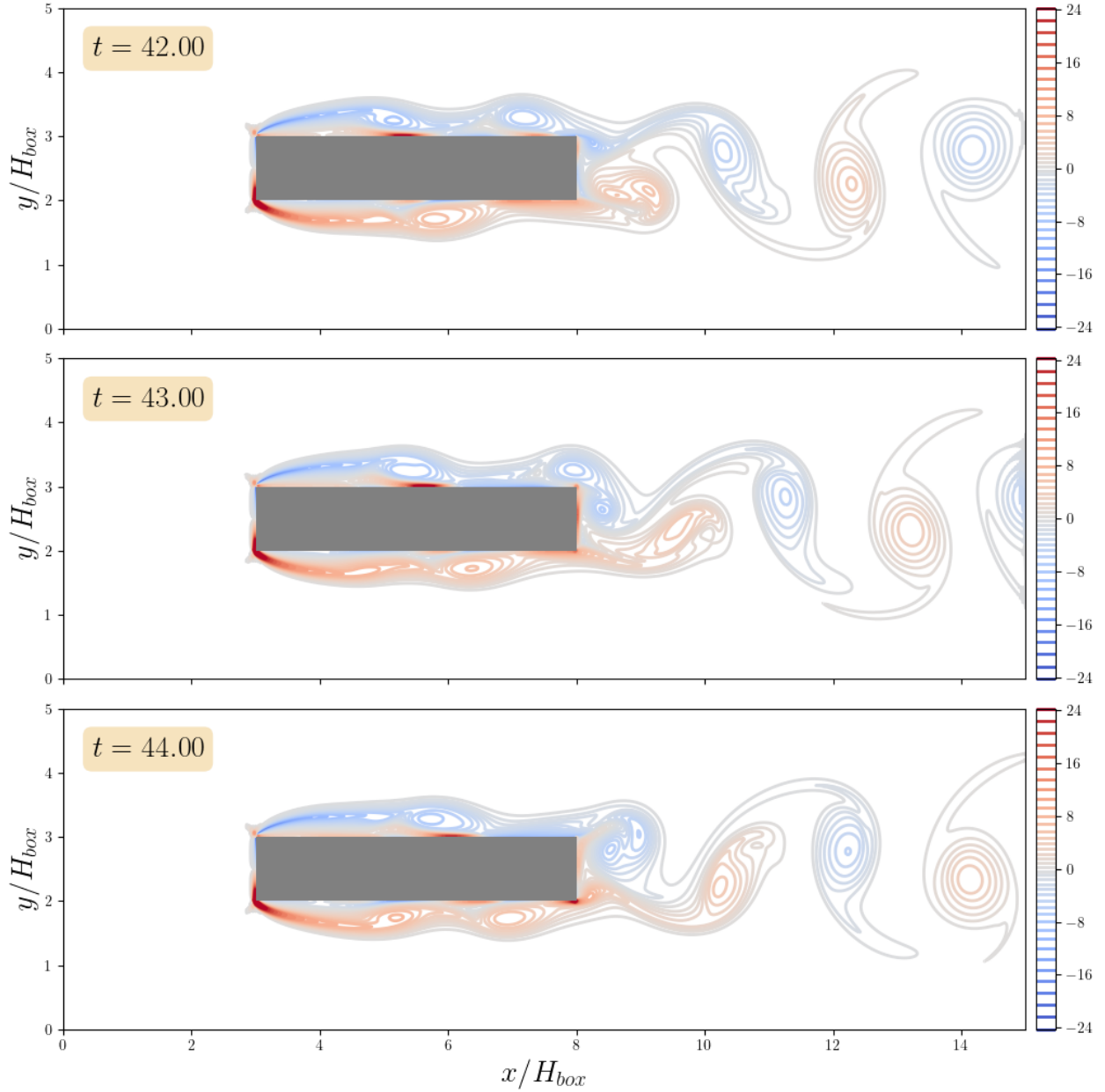
Figure 7. Level sets of the vorticity ω^* in *case 2* at different dimensionless times t.

Now, the flow is unsteady, but becomes periodic around $t = 10$. In this configuration, positive and negative vortices detach one after the other. In figure 7, we can observe a vortex, in blue above the rectangle detaching from the boundary layer. The delay between the ejection of a "positive" vortex ($\omega > 0$) and a "negative" vortex ($\omega < 0$) appears to be slightly more than 2 dimensionless times. We can call it the half-period, or $T/2$.
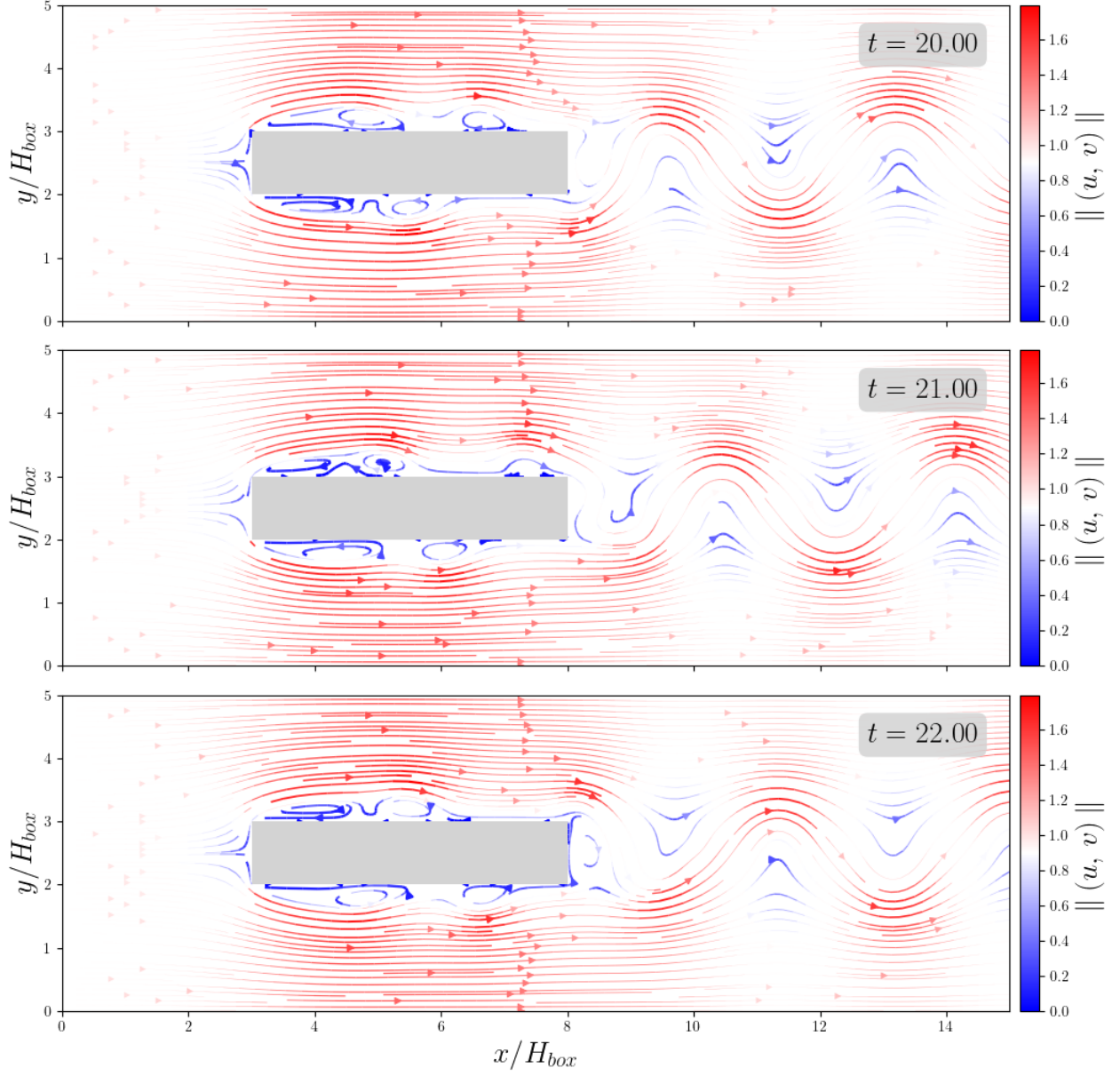
Figure 8. Streamlines of the flow in case 2 at different dimensionless times t.

In figure 8, we observe many small recirculation regions near the obstacle walls.

If we move away a little bit more from the upper and lower walls of the rectangle, we observe that the flow accelerates around the obstacle: this remark holds for all the cases.
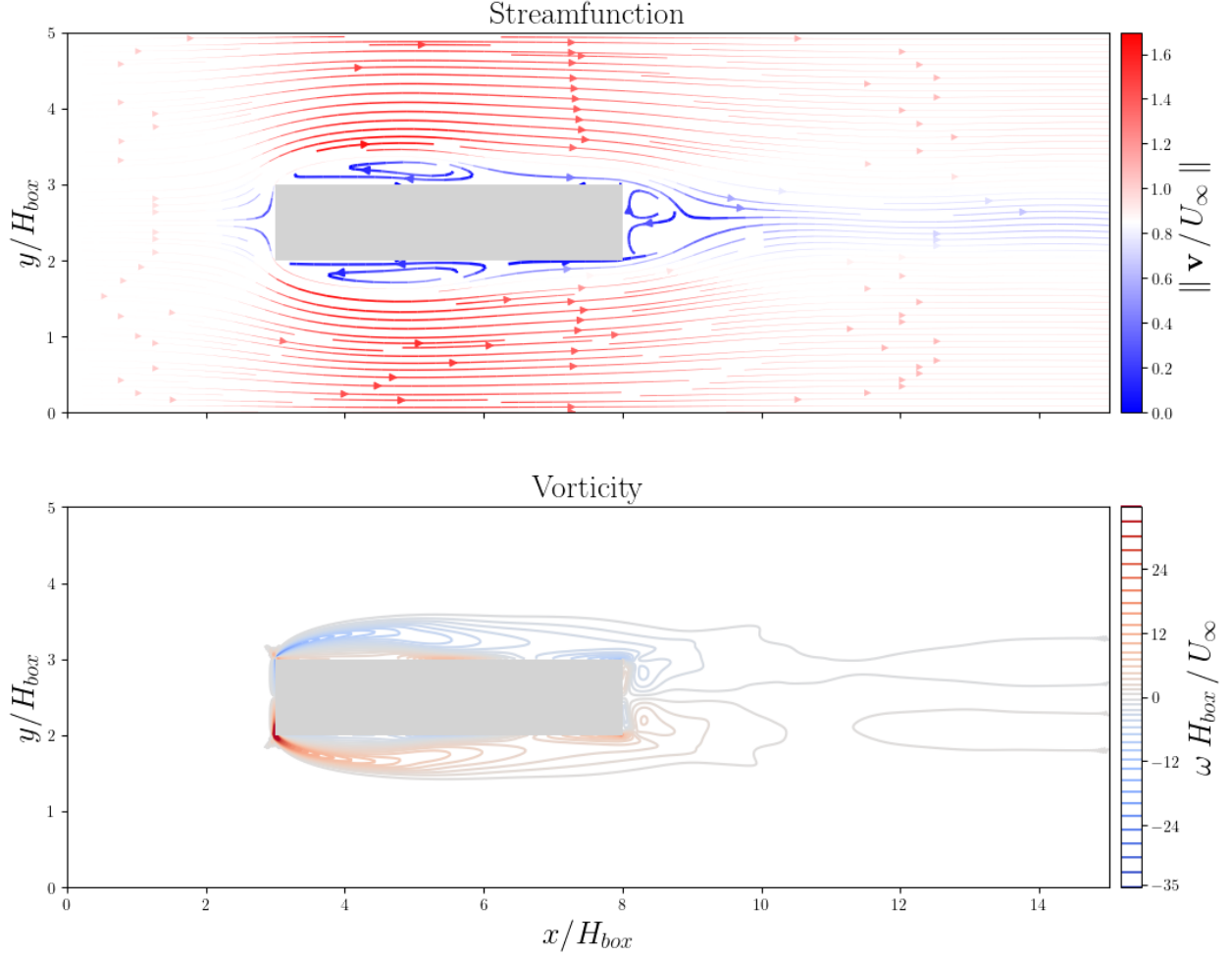
Figure 9. Streamlines and vorticity of the flow of *case 2* averaged from $t = 20$ to $t = 60$. The streamlines are the level sets the streamfunction $\psi/(U_\infty H_{box})$.

Looking the averaged-time flow in 9, we observe that the recirculation region is much smaller than in *case 1*: the *averaged stagnation point* is located ≈ 1 dimensionless unit behind the rectangle.

The mesh Reynolds number in 10 also oscillates with the half-period $T/2$ of the vortex shedding.

In figure 10, the drag coefficient C_d oscillates as well with that period $T/2$, while the lift coefficient oscillates with the full period T. This is because clockwise and anticlockwise vortices affect the drag in the same way, but they affect the lift in opposite ways.

Remark: the time axis of the aerodynamic coefficients stops at $t = 50$ and not $t = 60$ for a better visualization, but the flow was computed until $t = 60$.
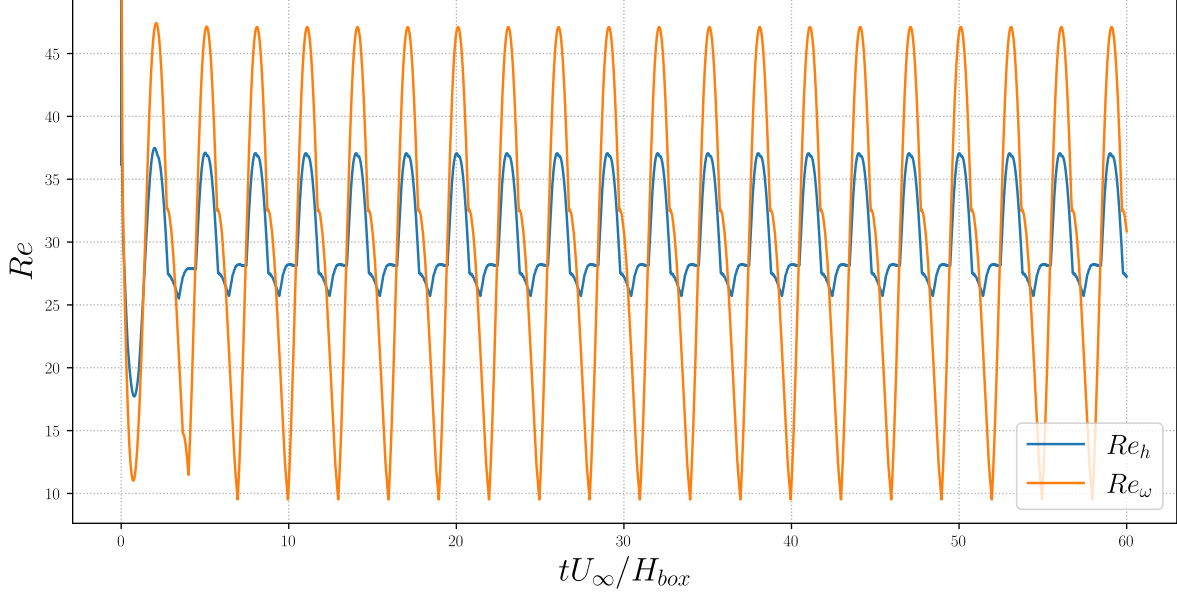
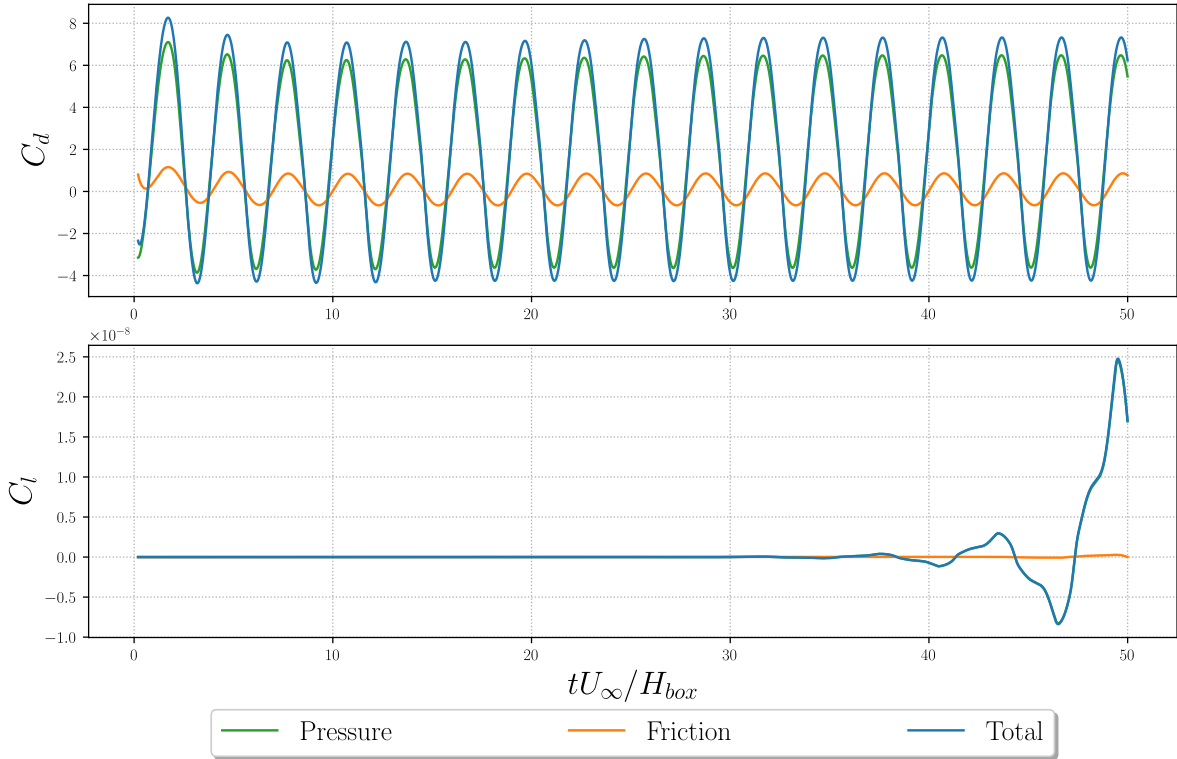**Figure 10.** Mesh Reynolds numbers evolution for *case 2*.
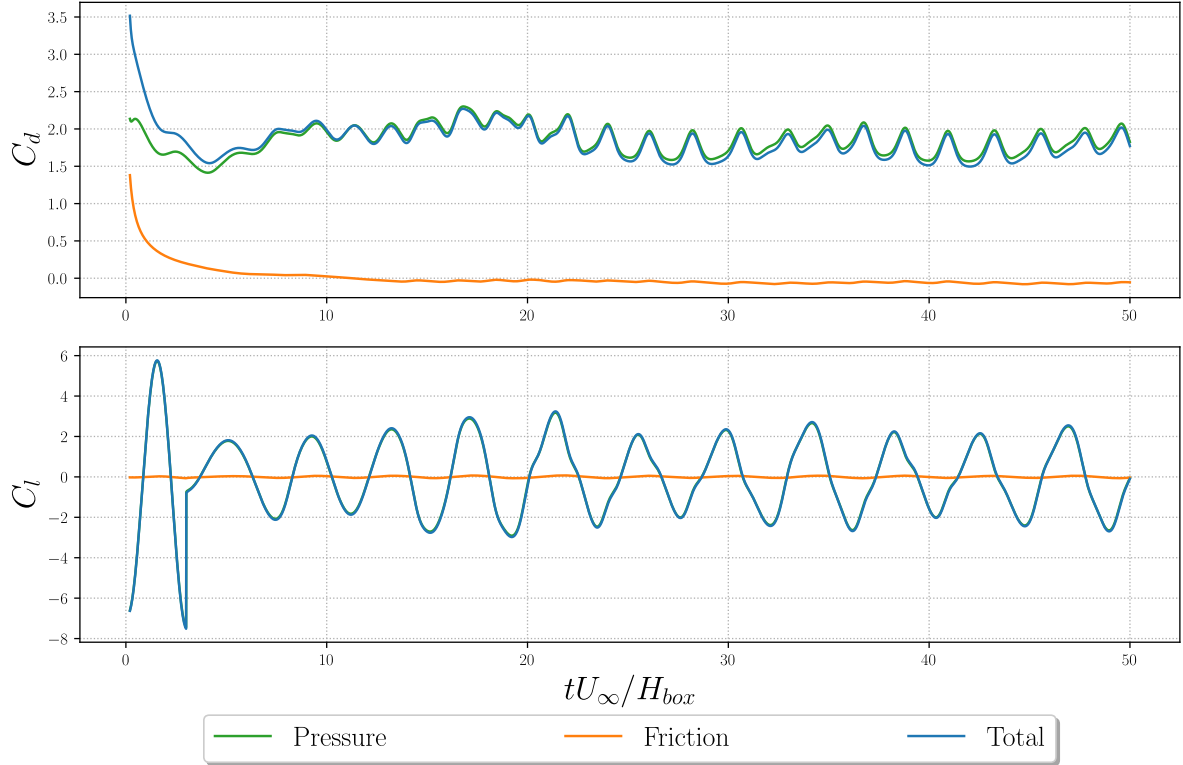
Figure 11. Aerodynamic coefficients evolution for *case 2*.

## 5.3   Case 3: obstacle oscillating with symmetrical flow
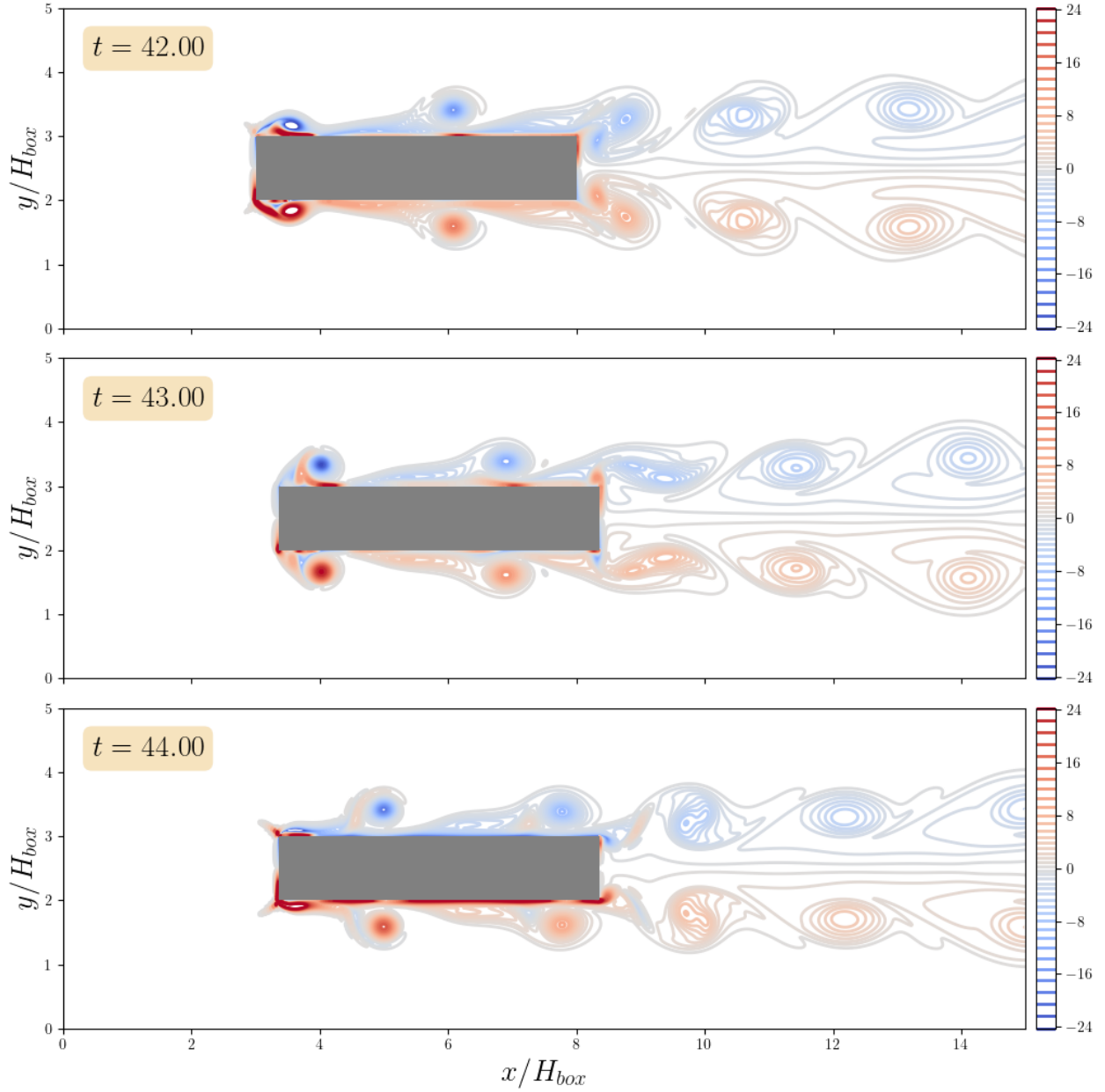
Figure 12. Level sets of the vorticity ω^* in *case 3* at different dimensionless times t.

The vorticity levels are shown in 12, at different times covering an oscillation period of the rectangle:

- at $t = 42$, the obstacle is at its leftmost position with maximum velocity headed to the right.
- at $t = 43$, the obstacle has almost reached its rightmost position, still moving to the right, but slowing down.
- at $t = 44$, the obstacle is now moving to left, reaching the same position as at $t = 43$.

Vortices are generated around the upper left and lower left corners of the obstacle at $t = 0 \bmod 3$, before *sliding* close to the wall and finally detaching.

Two remarks about figure 14:

- The lift coefficient C_l is again zero since the flow is symmetrical, as in *case 1*.
- Both the the pressure drag and friction drag can become negative: when the box is accelerating to the right, the fluid resists this motion and *pushes* the box to the left.

Figure 13. Mesh Reynolds numbers evolution for *case 3*.

Figure 14. Aerodynamic coefficients evolution for *case 3*.

5.4 Case 4: obstacle oscillating with unsymmetrical flow
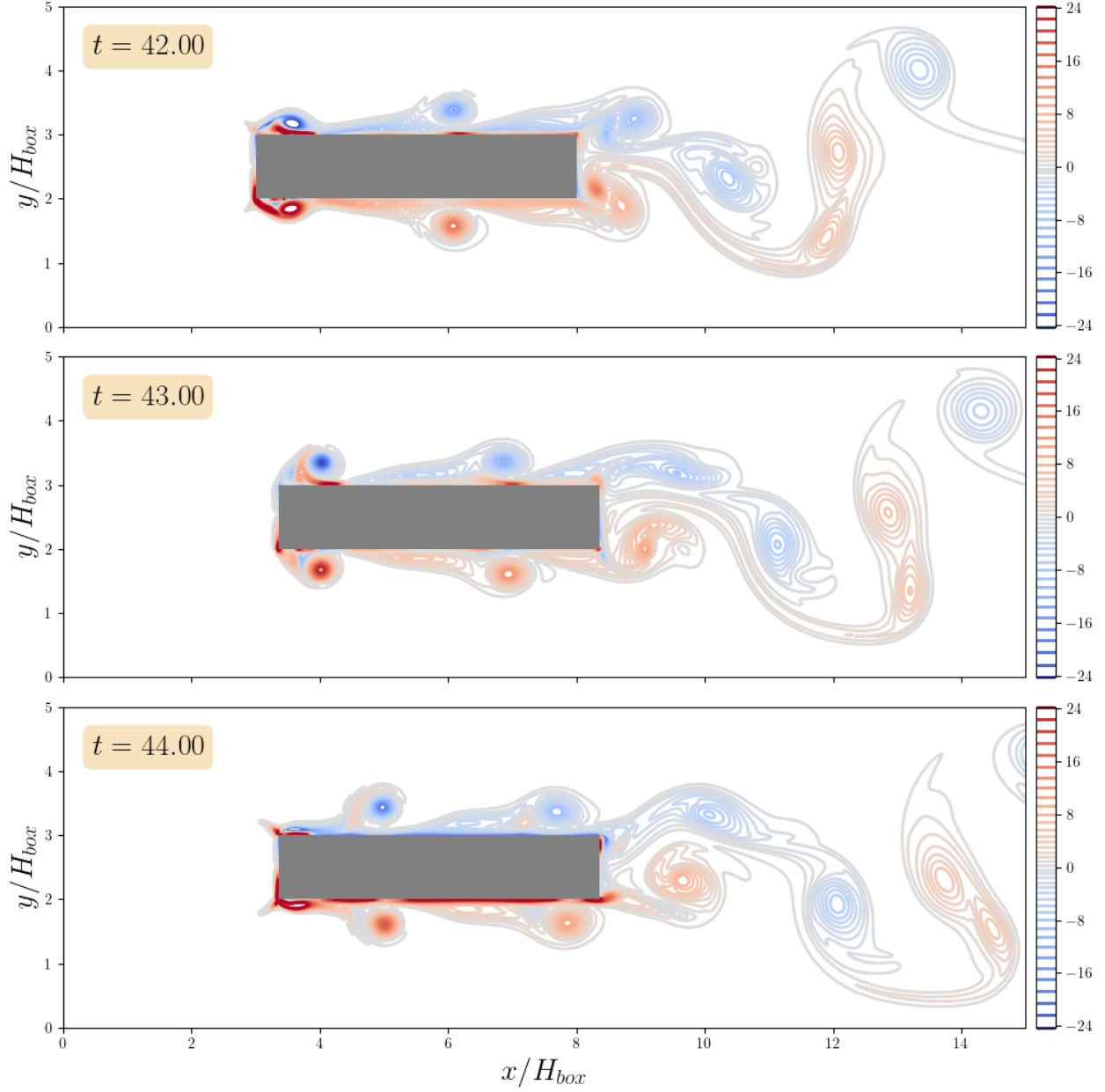
Figure 15. Level sets of the vorticity ω^* in *case 4* at different dimensionless times t.

Now, thanks to the vertical perturbation, we obtain a non-symmetrical vortex shedding. In figure 15, the vorticity field is shown at the same times as for *case 3* - figure 12. As opposed to the *case 2*, we see that the vortices come by pair: one generated upstream due to the friction along the wall, the other one generated downstream behind the obstacle.
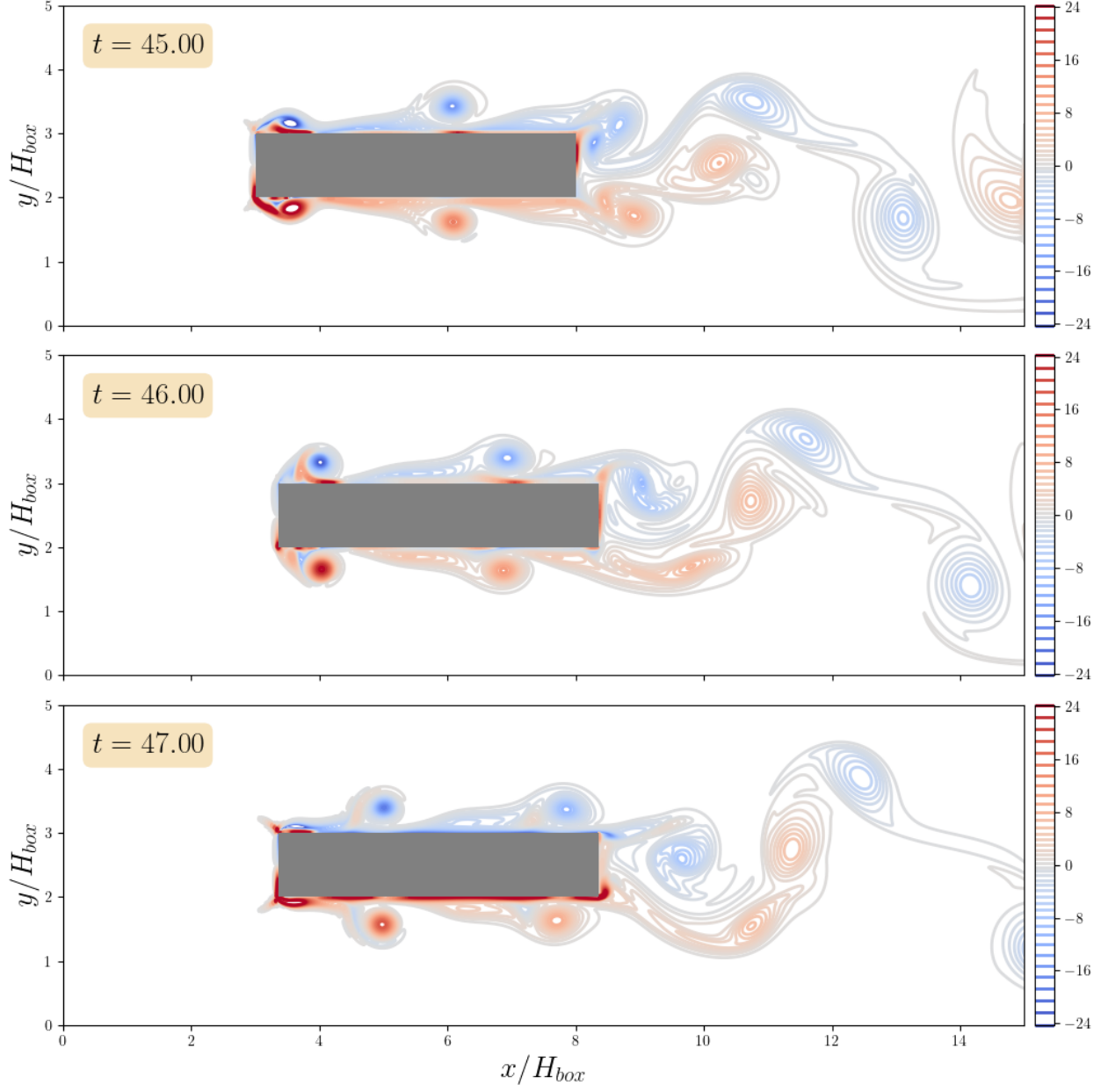
Figure 16. Level sets of the vorticity ω^* in *case 4* at different dimensionless times t - continued.

In figure 16, the field is shown for three more dimensionless times $t = 45, 46, 47$. This shows that the period of the vortex shedding is twice the period of the rectangle oscillation.
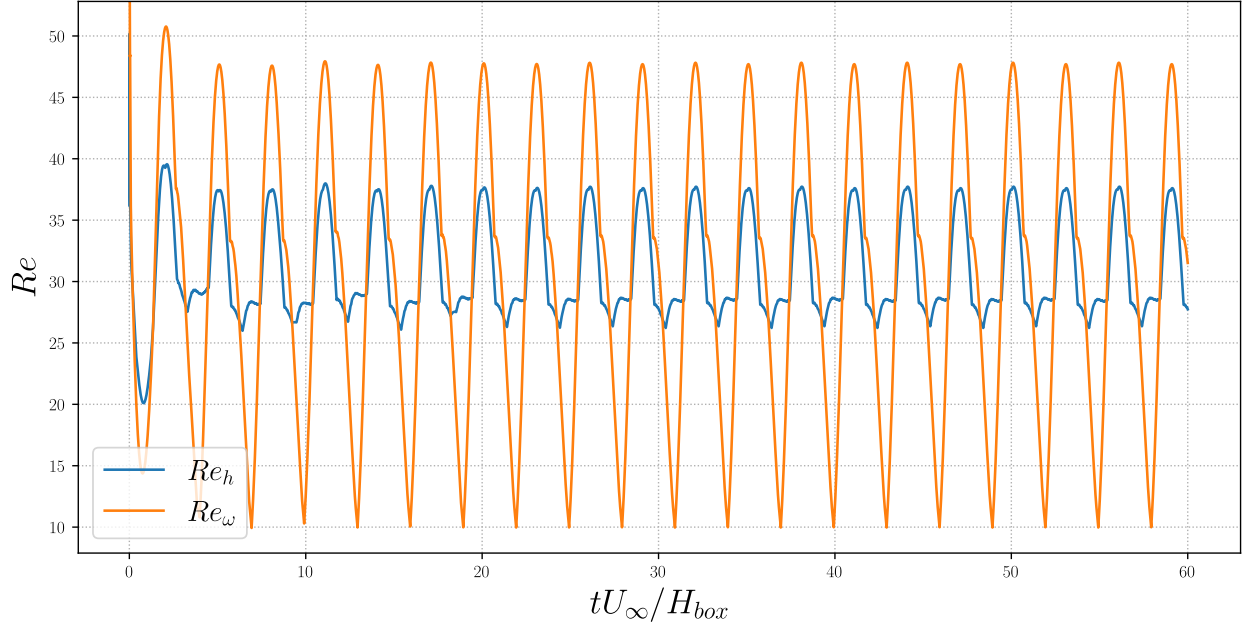
Figure 17. Mesh Reynolds numbers evolution for *case 3*.
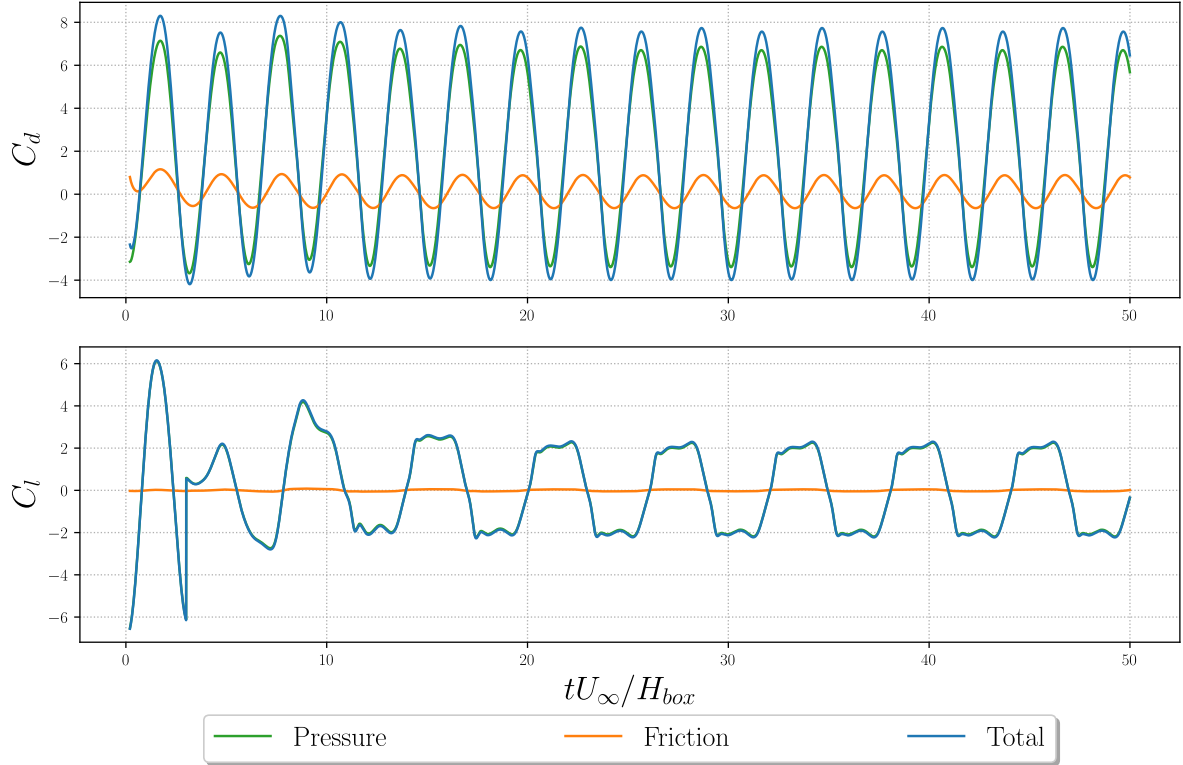
Figure 18. Aerodynamic coefficients evolution for *case 4*.

6 Simulations with temperature coupling

6.1 Hot obstacle

In this situation, the obstacle walls are maintained at a fixed dimensionless temperature $T = 1$. For all the other walls, an adiabatic boundary condition is used.
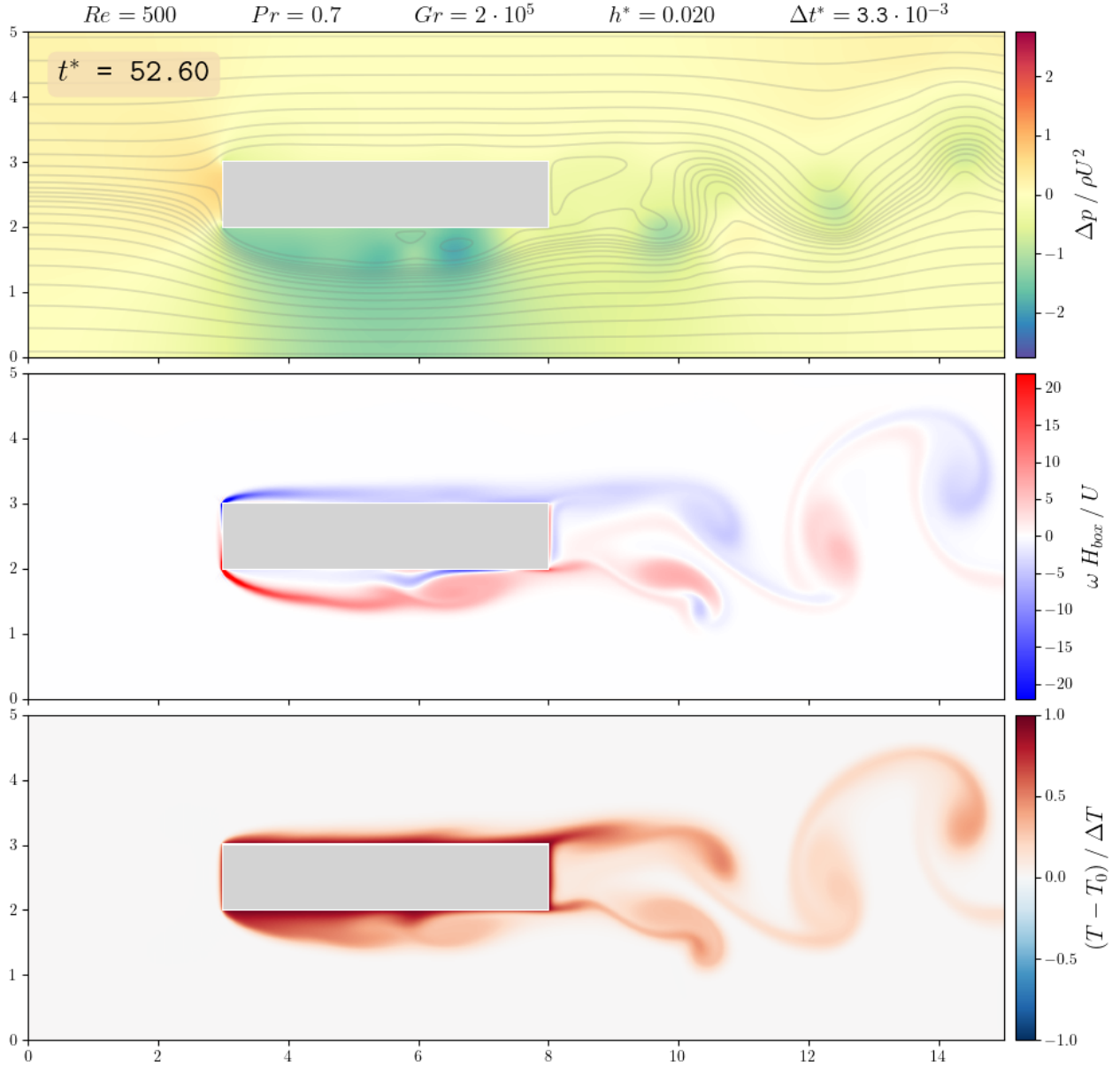
Figure 19. Streamlines, pressure, vorticity and temperature fields.
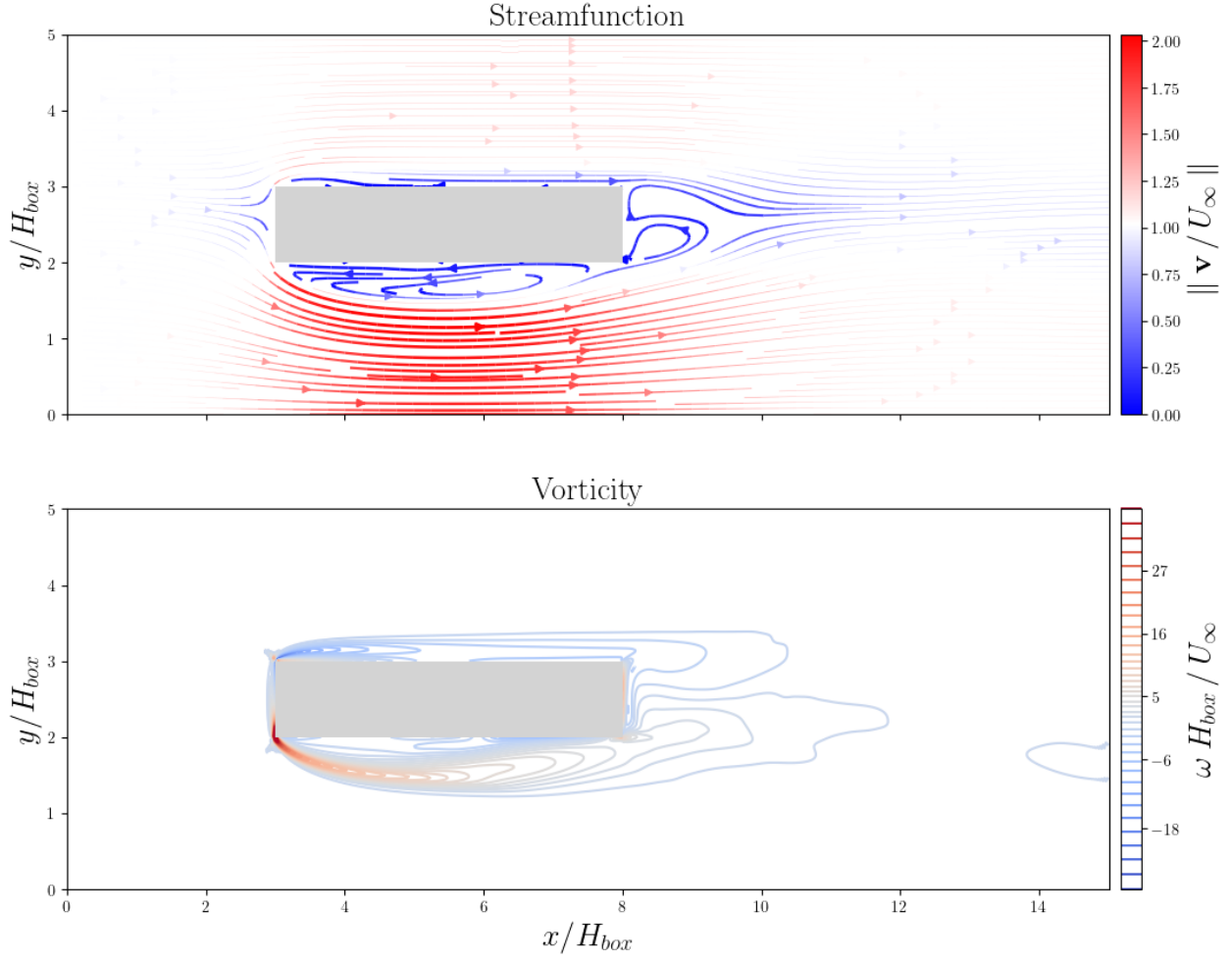
Figure 20. Streamlines and vorticity of the flow averaged from $t = 20$ to $t = 60$.

Due to the buoyancy, the fluid located underneath the obstacle accelerates more than the fluid above as shown in figure 20. The pressure differential related to this acceleration can also be seen in the lift coefficient that becomes seriously negative in figure 22.
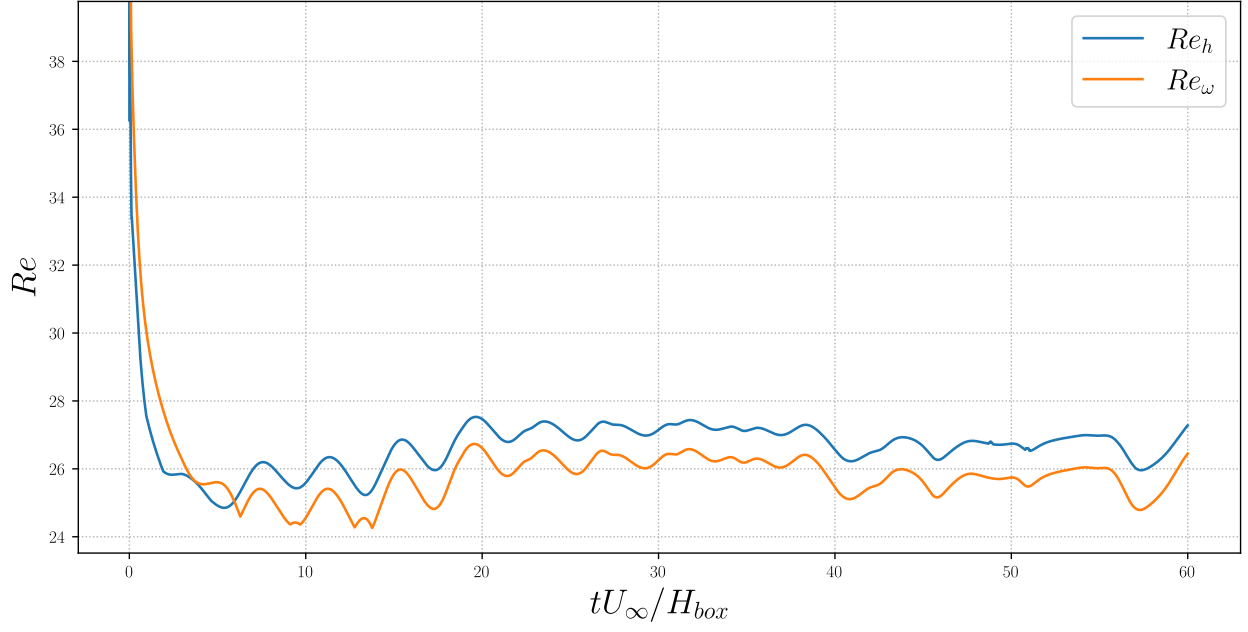
Figure 21. Mesh Reynolds numbers evolution.
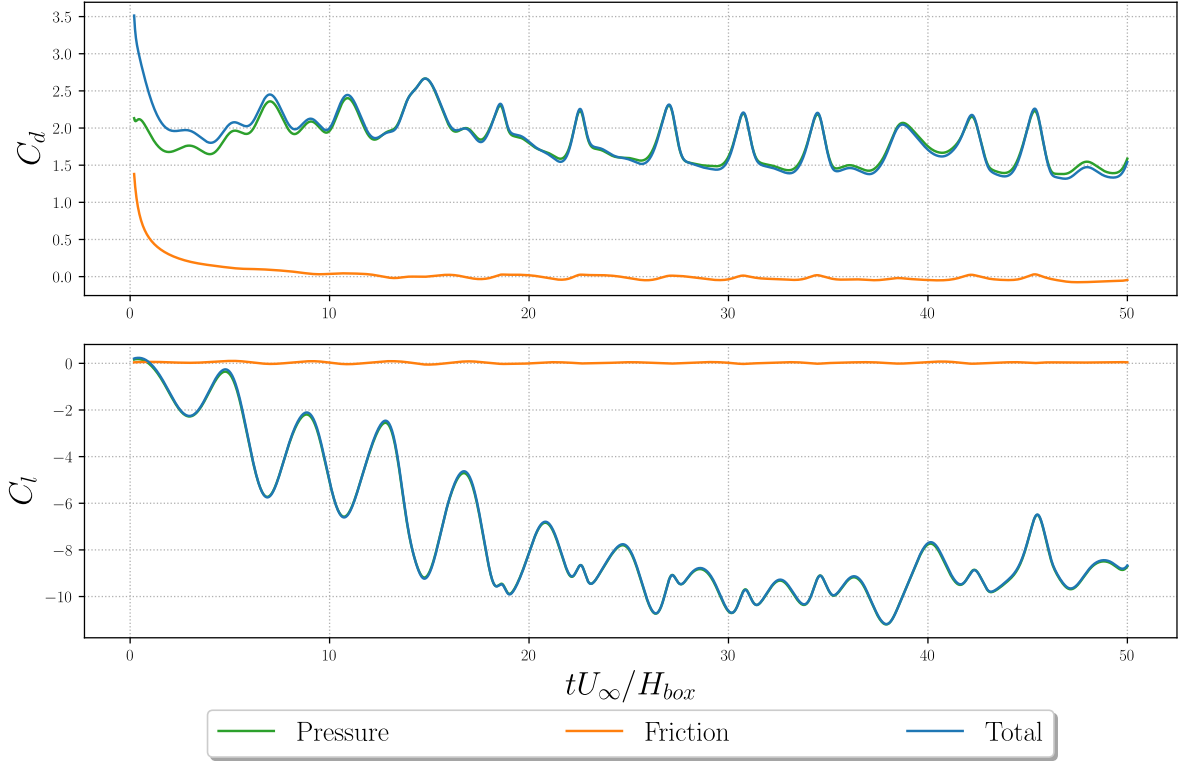
Figure 22. Aerodynamic coefficients evolution.

6.2 Obstacle cold above and hot underneath

In this situation, the obstacle upper wall is maintained at a fixed dimensionless temperature $T = -0.8$, the wall underneath at $T = 1.$. For all the other walls, including the lateral walls of the obstacle, the boundary condition is adiabatic.
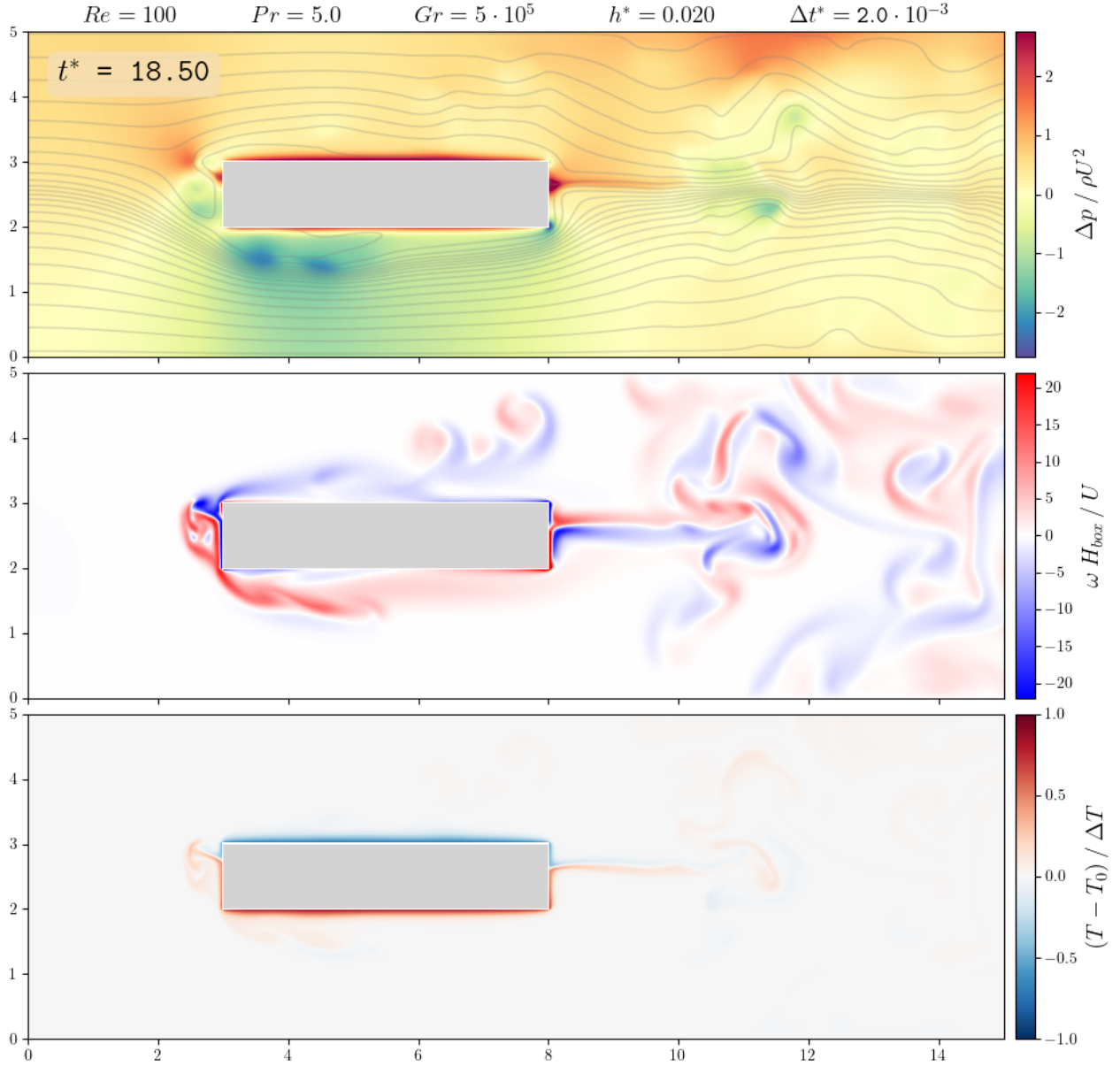

Figure 23. Streamlines, pressure, vorticity and temperature fields.

Since $Pr = 5 \gg 1$, the thermal boundary layer is much smaller than the velocity boundary layer. Furthermore, since the temperature is non-symmetrical ($|-0.8| < |1|$), there are sometimes hotter regions that are able to go upstream and to reach the other side of the obstacle.
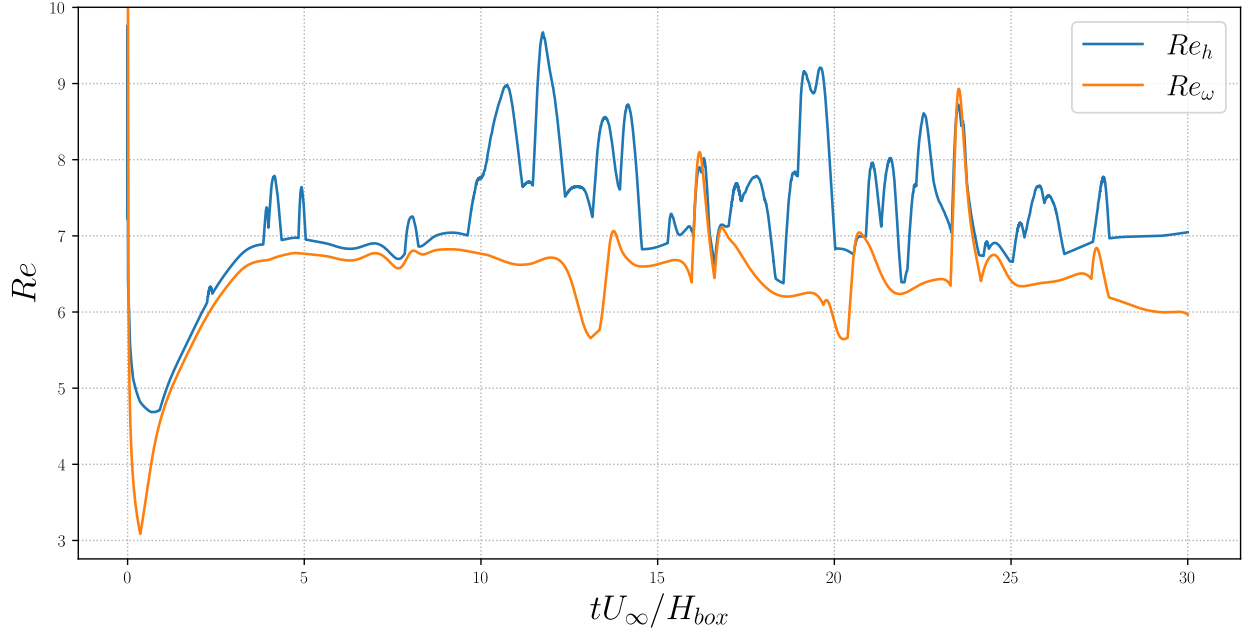
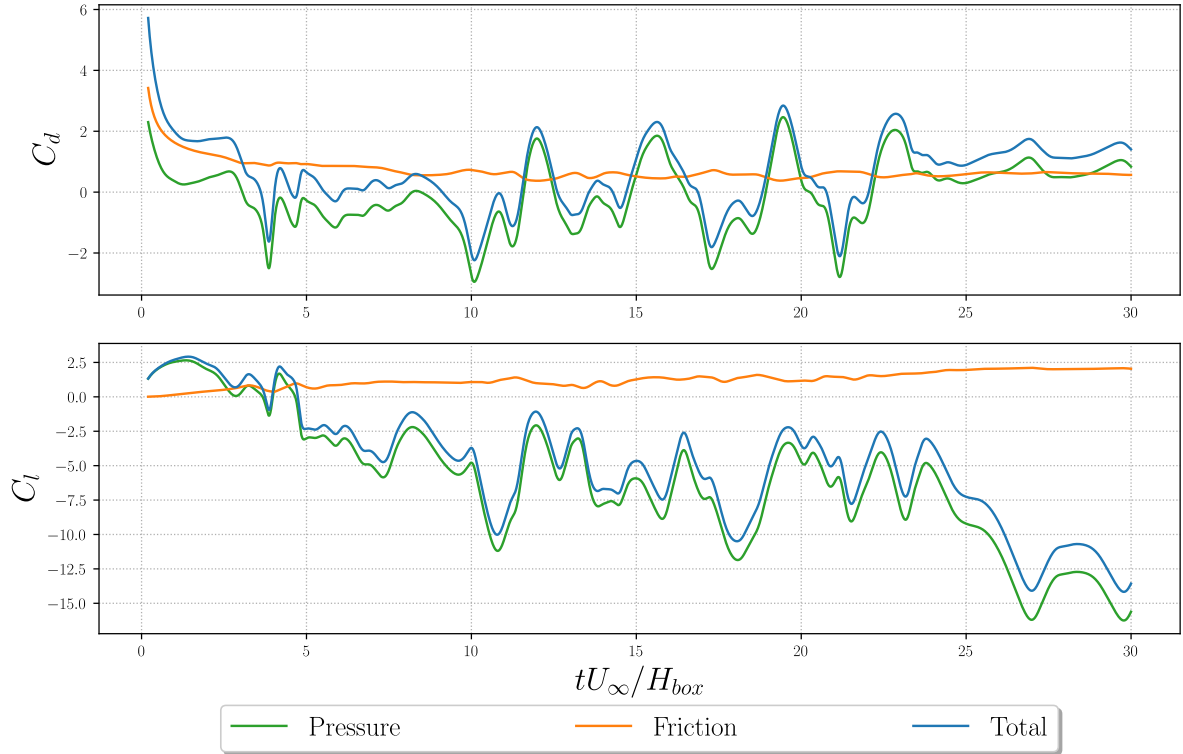**Figure 24.** Mesh Reynolds numbers evolution.

Figure 25. Aerodynamic coefficients evolution.

6.3 No-slip walls with fixed temperature

In this situation, the external walls become real walls, with a no-slip condition enforced. Furthermore, the upper and lower walls are respectively maintained at dimensionless temperature $T = -1$ and $T = 1$ to produce more convection. All the other walls are considered adiabatic.
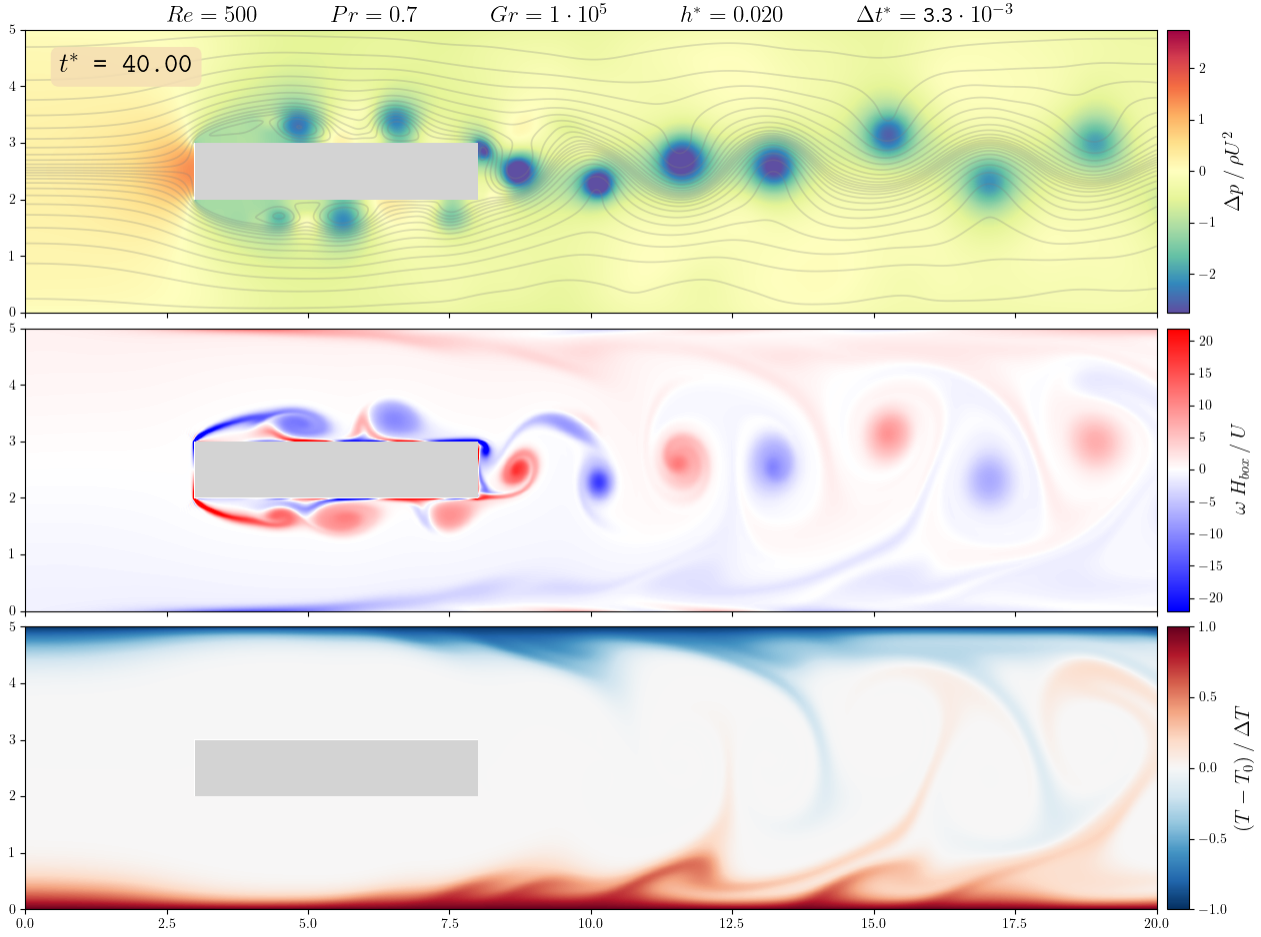

Figure 26. Streamlines, pressure, vorticity and temperature fields.

With the no-slip boundary condition, we must be careful concerning the outflow boundary condition for higher values of Gr. In fact, when $Gr > 5 \cdot 10^5$, the flow becomes more complex and vortices become strong enough that the horizontal velocity u sometimes is negative near the outflow. When these strong vortices reach the right boundary of Ω, they are *stuck* inside the domain. An example is given in the video `anim/no_slip_crash.mp4`.

Therefore, I imposed a zero mass flow, and set u_c with a Poiseuille profile. But these corrections do not seem to improve the situation. The bug can be observed in another video: `anim/no_slip_problem.mp4`.
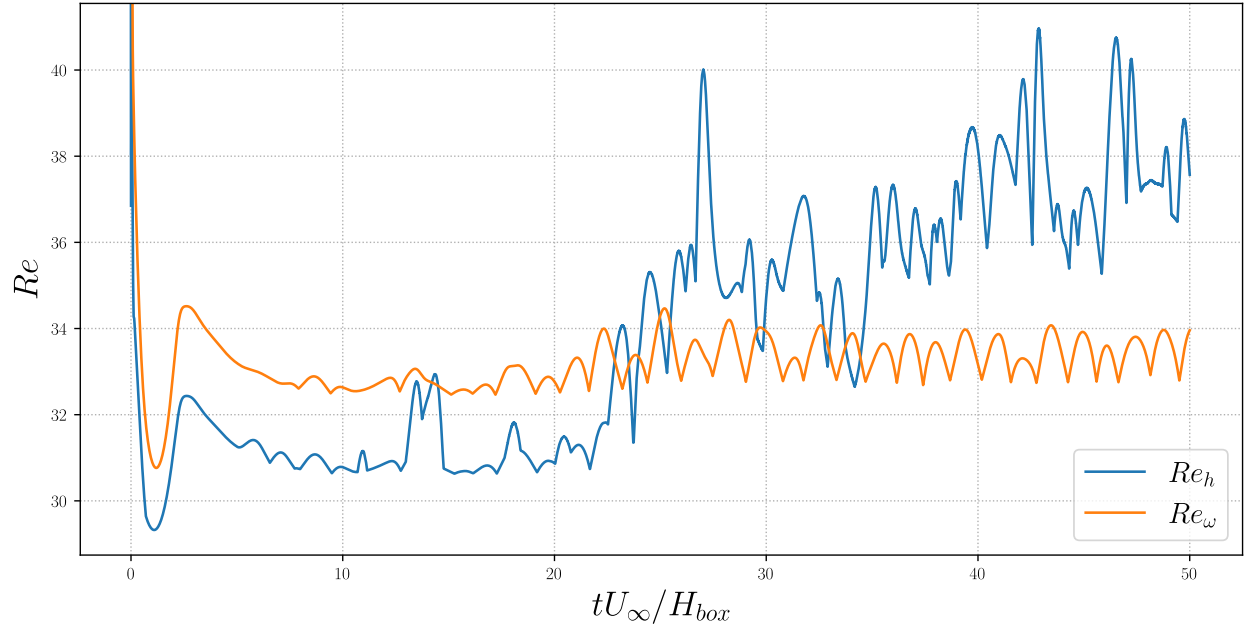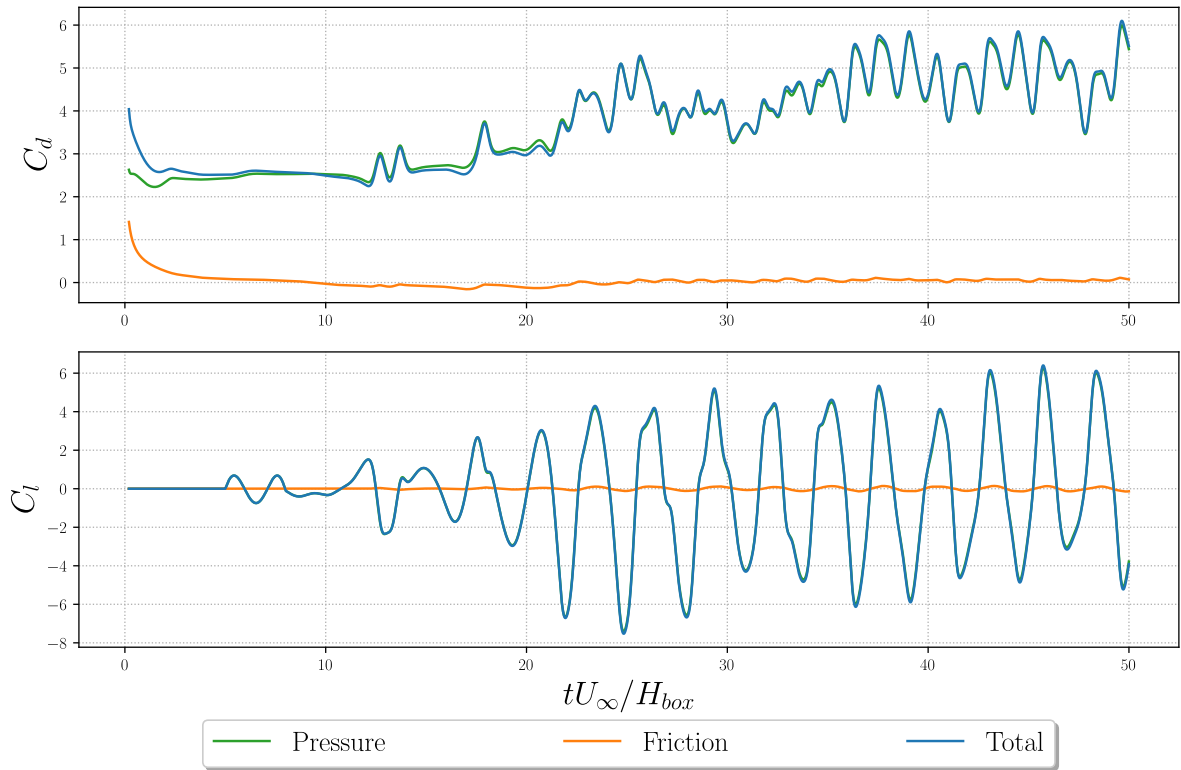
Figure 27. Mesh Reynolds numbers evolution.

Figure 28. Aerodynamic coefficients evolution.

6.4 Heat generation through viscous dissipation

In this situation, all the walls are considered adiabatic. The heat source is only the viscous dissipation ϕ.
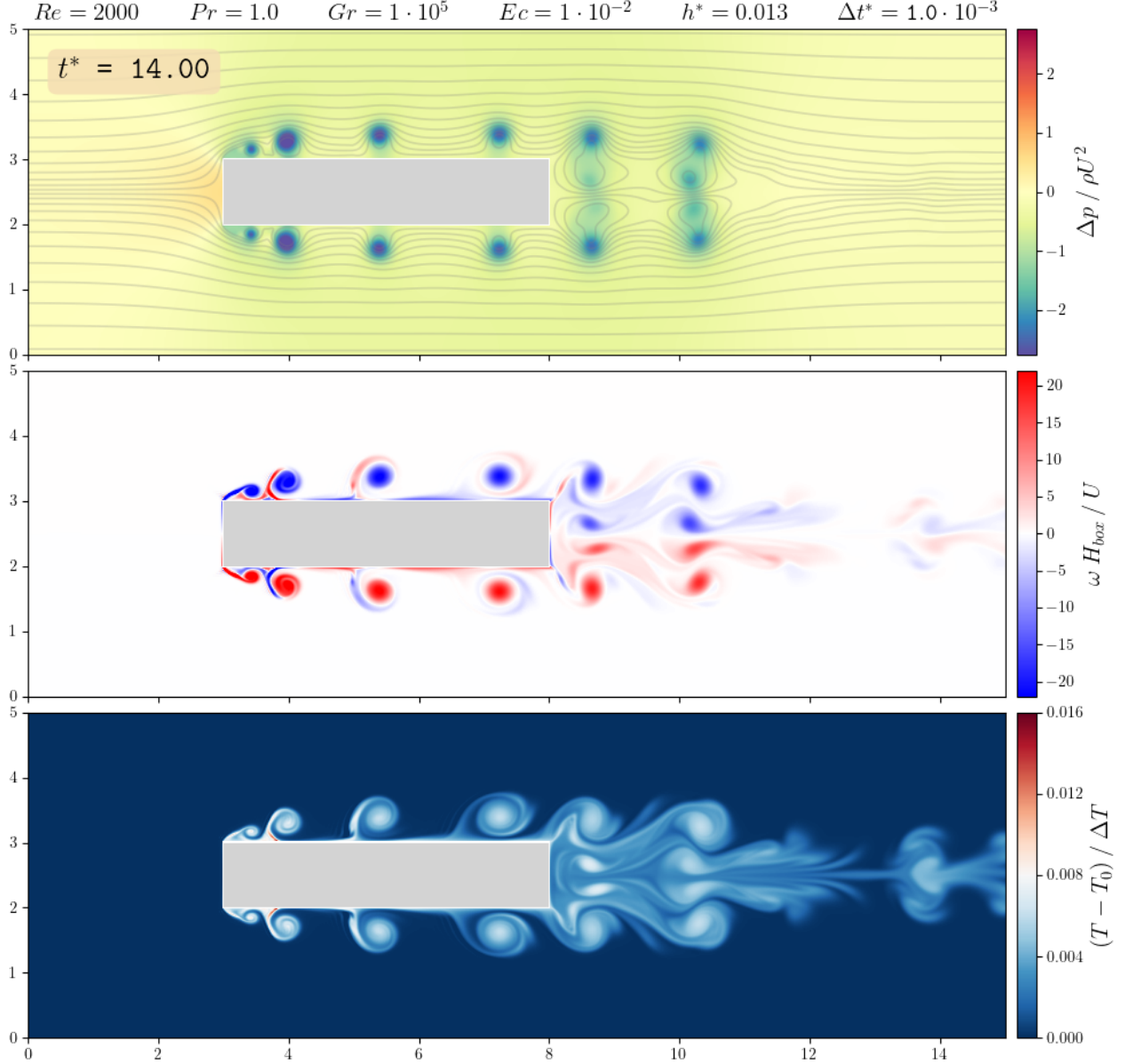

Figure 29. Streamlines, pressure, vorticity and temperature fields.

In figure 29, the flow is about to become unsymmetrical due to the buoyancy effect ($Gr = 10^5$). It took that much time $t \approx 14$ to break the symmetry since $T \ll 1$.

In this situation, we consider a higher Reynolds number: $Re = 2000$. But, even with a spatial step $h = \frac{1}{80} H_{box}$, the mesh Reynolds number is too large ≈ 80. A stretched grid near the obstacle would allow us to compute such flows with more precision.
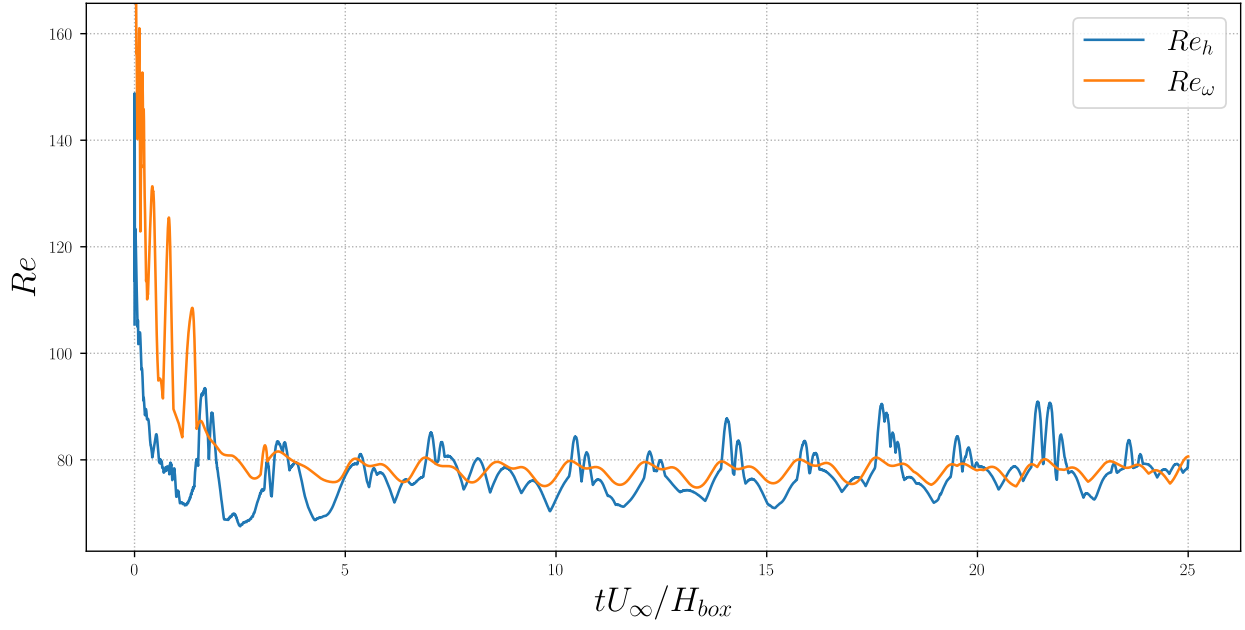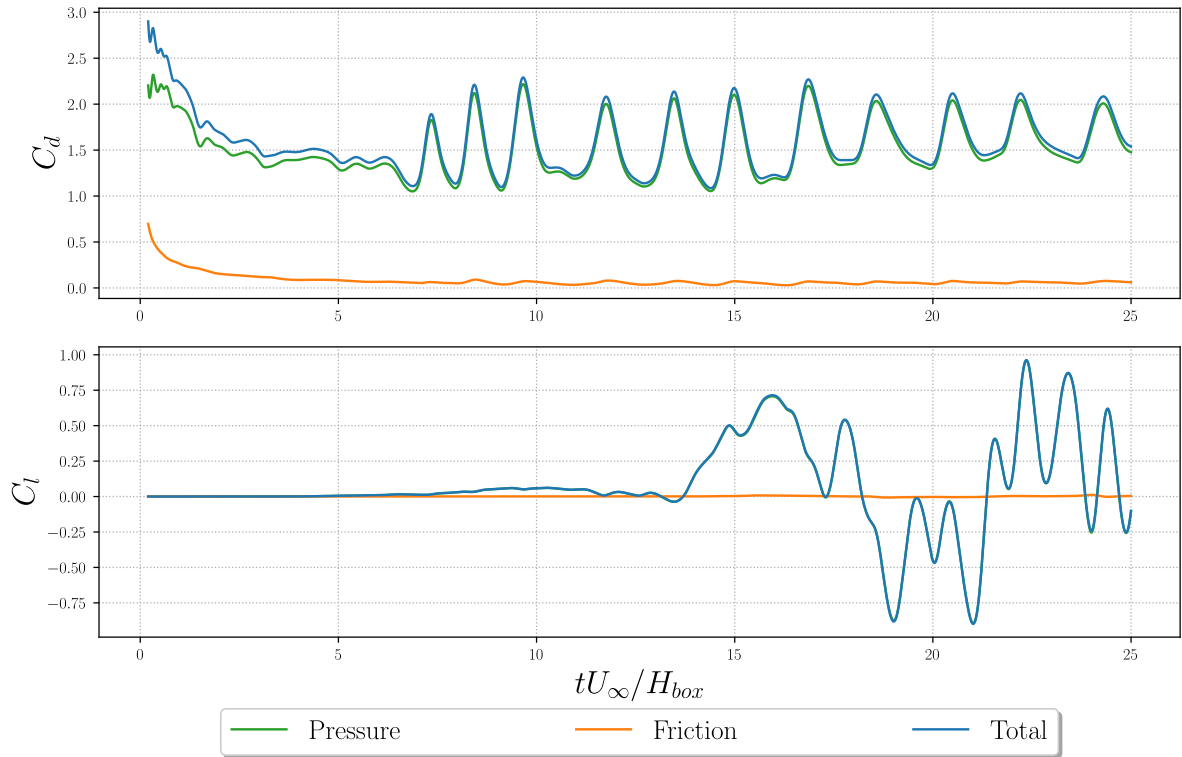
Figure 30. Mesh Reynolds numbers evolution.

Figure 31. Aerodynamic coefficients evolution.

26

References

[1] Satish Balay, William D. Gropp, Lois Curfman McInnes, and Barry F. Smith. Efficient management of parallelism in object oriented numerical software libraries. In E. Arge, A. M. Bruaset, and H. P. Langtangen, editors, *Modern Software Tools in Scientific Computing*, pages 163–202. Birkhäuser Press, 1997.

[2] K.A. Hoffmann and S.T. Chiang. *Computational Fluid Dynamics*. Number vol. 1 in Computational Fluid Dynamics. Engineering Education System, 2000.

[3] G. Winckelmans. *LMECA2660 - Finite differences convection diffusion [Course notes]*. EPL, 2018.